
Unterschrift des Betreuers



DIPLOMARBEIT

Process Quality Control of Silicon Strip Detectors for the CMS Tracker

ausgeführt am

Institut für Hochenergiephysik
der Österreichischen Akademie der Wissenschaften

und am

Atominstitut
der Österreichischen Universitäten

unter Anleitung von

Univ.Doiz. Dipl.-Ing. Dr.techn. Manfred KRAMMER

durch

Thomas Bergauer

Spengergasse 43/20
1050 Wien

2. August 2004

Unterschrift

Preface

This diploma thesis has been developed at the Institute for High Energy Physics (HEPHY) of the Austrian Academy of Sciences [1], which is involved in the construction of the CMS Tracker, a particle detector currently built at CERN, Geneva (CH). Since the requirements for CMS are very challenging, a large number of institutes and people are involved in the assembly and tests of all components the apparatus consists of. The results of my work on silicon sensors are presented in this thesis.

Chapter 1 gives a short overview of the LHC accelerator and the physics aims. The CMS experiment is described in Chapter 2. Its central element is the Silicon Strip Tracker, whose principal components – silicon strip sensors – are presented in detail in Chapter 3.

The systems I have contributed in terms of design, construction and operation are described in Chapter 4 and 5. The aim of the system presented in Chapter 4 is to determine characteristic semiconductor parameters to assure a stable production process of the silicon sensors. First, an overview of the hardware is given, while in the following section the various measurements are described in detail. A theoretical introduction and the experimental solution with the electrical scheme is given for every measurement. After almost two years of operation, a huge number of data has been accumulated. The evolution of every measured parameter is shown in the end of this chapter and compared between the two producers of silicon sensors.

Chapter 5 is about the longterm stability of the silicon sensors at room temperature and its operation at -10°C . The electrical scheme and the measurement setup are described first, while the results are discussed afterwards.

The overall summary is given in Chapter 6.

Contents

1	The Large Hadron Collider	6
1.1	Machine Overview	6
1.2	Physics Aims	8
1.2.1	The Higgs Particle	8
1.2.2	CP Violation	10
1.2.3	Quark-Gluon-Plasma	11
2	The CMS Experiment	12
2.1	The Superconducting Magnet	14
2.2	Inner Tracker	14
2.3	Calorimetry	15
2.3.1	Electromagnetic Calorimeter	15
2.3.2	Hadronic Calorimeter	16
2.4	Muon System	16
3	The CMS Silicon Strip Sensors and their Qualification Procedure	18
3.1	Energy Loss	18
3.2	Charge Collection	19
3.3	Silicon Sensor Characteristics	22
3.4	Radiation Damage	24
3.5	Tracker Geometry	25
3.6	Sensor Design	26
3.7	The Sensor Quality Assurance	28
3.8	The Tracker Database	29
4	Process Quality Control	30
4.1	Measurement Setup	30
4.2	Description of Measurements	33
4.2.1	Coupling Capacitance (C_{ac})	33
4.2.2	Dielectric Breakdown (IV_{diel})	36
4.2.3	Flatband Voltage (CV_{MOS})	37
4.2.4	Surface Current I_{surf} and Gate Controlled Diode (IV_{GCD})	41
4.2.5	Sheet Resistances	44
4.2.6	Interstrip Capacitance (C_{int})	46
4.2.7	Depletion Voltage and Resistivity (CV_{diode})	48
4.2.8	Dark Current and Breakthrough (IV_{baby})	51

4.2.9	Interstrip Resistance (R_{int})	53
4.3	Measurement Procedure and Software	55
4.4	Measurement Results	57
4.4.1	Coupling Capacitance C_{ac}	57
4.4.2	Dielectric Current I_{diel}	57
4.4.3	Flatband Voltage V_{fb}	58
4.4.4	Surface Current I_{surf}	59
4.4.5	Sheet Resistances	59
4.4.6	Interstrip Capacitance C_{int}	61
4.4.7	Depletion Voltage V_{depl}	61
4.4.8	Dark Current I_{tot}	62
4.4.9	Interstrip Resistance R_{int}	62
4.5	Summary of the Results	63
5	Long Term Stability Tests	64
5.1	Measurement Setup	64
5.1.1	Setup Description	64
5.1.2	Results	67
5.2	Longterm Tests at Operating Temperature	70
5.2.1	Setup Description	70
5.2.2	Results	71
5.3	Summary	72
6	Summary	73
6.1	Process Quality Control	73
6.2	Longterm Validation	74
6.3	Conclusion	74
	Acknowledgements	75
	Appendix	76
A	PQC Tables	76
A.1	Wiring Scheme	76
A.2	Input File	81
B	LTV Tables	83
B.1	Input File	83
	Bibliography	85

Für meine Eltern.

Chapter 1

The Large Hadron Collider

Particle accelerators are the physicists microscope. By accelerating two independent particle beams in opposite directions and bringing them to collision, a variety of new particles is created which are not part of our "macroscopic" life. Physicists are interested in these new particles, since they help to understand the universe and its conditions shortly after the big bang, about 10 to 15 billion years ago.

The correlation between theoretical prediction and experimental measurement of these particles led to a sophisticated theory called the "Standard Model" of particle physics. So far, the Standard Model was successful, but open issues at high energy remain. Stronger accelerators are necessary to prove its validity also in this region. For this reason, the idea of the *Large Hadron Collider* (LHC) was born.

1.1 Machine Overview

The LHC will be the world's largest particle accelerator. It is currently under construction in the former LEP¹ tunnel at CERN [2] and will become operational in 2007.

The LHC will use some of the smaller machines of the CERN accelerator complex as injector systems [3]: After the production of protons or lead ions in the sources, the particles traverse the *Linear Accelerators* (LINACs), the *Proton Synchrotron Booster* (PSB), the *Proton Synchrotron* (PS) and the *Super Proton Synchrotron* (SPS). The pre-accelerated particles with an energy of 450 GeV are transported to the LHC machine in the transfer lines (fig. 1.1).

Because of its colliding beams, a particle accelerator of that type is called *collider*. It has the advantage that the particle interaction can be observed in the center-of-mass system, where the total energy of the beams can be used for particle generation. In another type of accelerator a particle beam hits a fixed target, where the energy available for particle generation scales with the square root of the beam energy. Thus, a collider is mandatory to reach highest energies. Its center-of-mass energy E_{cm} is the sum of the

¹Large Electron Positron Collider

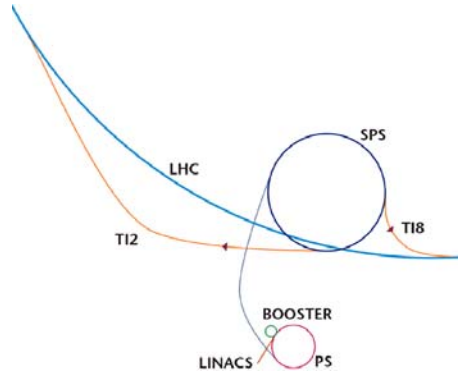


Figure 1.1: The pre-acceleration and insertion of the particles into the LHC machine.

energies of both particle beams E_{Beam} , which is 14 TeV in the case of protons in the LHC. In the ion-ion collision mode, the energies are even higher.

The collision rate R in a collider is proportional to the interaction cross-section σ_{int} ,

$$R = \mathcal{L} \sigma_{\text{int}} \quad , \quad (1.1)$$

with the factor \mathcal{L} called luminosity [4]. When two bunches, each containing n particles, collide with the frequency f , the luminosity is given by

$$\mathcal{L} = f \frac{n^2}{4\pi\sigma_x\sigma_y} \quad (1.2)$$

where σ_x and σ_y characterize the beam spreads in horizontal and vertical directions.

An overview of the characteristic parameters of LEP and LHC is given in tab. 1.1.

Machine	Particles	E_{cm} [TeV]	\mathcal{L} [cm ⁻² s ⁻¹]	t_{bunch} [ns]	R [1/s]
LEP	e ⁺ / e ⁻	0.2	10 ³²	22000	1
LHC	p / p	14	10 ³⁴	25	7.2 · 10 ⁸
LHC	Pb / Pb	1312	10 ²⁷	125	5 · 10 ³

Table 1.1: Properties of LHC and its predecessor LEP. The different operation modes for protons and lead ions of the LHC are shown separately.

Four detectors will be located at the collision points along the circular LHC. These are called *experiments* and can be divided into two groups: Two large multi-purpose experiments called ATLAS (A *Toroidal LHC Apparatus*) and CMS (*Compact Muon Solenoid*), and two smaller experiments with very dedicated intentions: LHCb to study the CP violation of B-mesons and ALICE (A *Large Ion Collider Experiment*). The position of these experiments along the LHC tunnel is shown in fig. 1.2 While ATLAS, CMS and LHCb use $p - p$ interactions, ALICE is an experiment which uses the other operational mode of LHC. In that mode, ions – mostly lead (Pb) – are accelerated to study the physics of strongly interacting matter at extreme densities where the formation of quark-gluon plasma is expected [5].

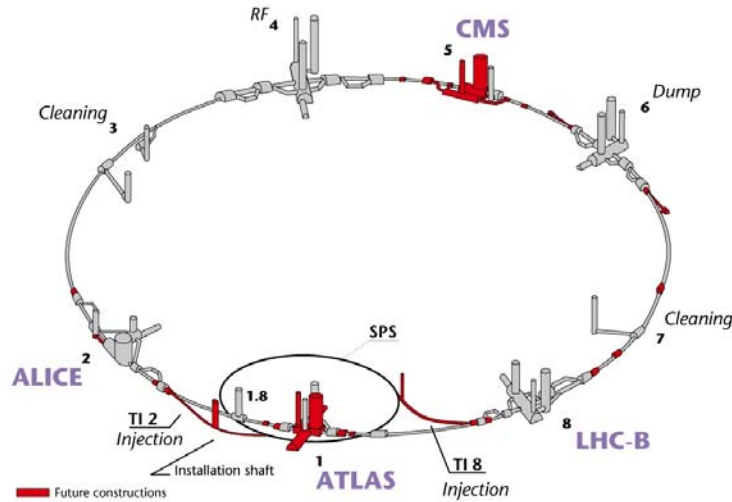


Figure 1.2: The four experiments of the LHC. The position of ATLAS is called Point 1, while ALICE resides at Point 2, CMS at Point 5 and LHC-B at Point 8.

1.2 Physics Aims

1.2.1 The Higgs Particle

Particle physics has two main goals: to find and determine the properties of the ultimate constituents of matter and to investigate the forces through which these interact. In the Standard Model the building blocks of matter are called fermions and the forces are described by exchange bosons. The fermions have spin $1/2$ while the bosons are spin-1 particles.

Matter only consists of two types of building blocks, quarks and leptons, which are arranged in three generations. For leptons, each generation consists of a particle of charge -1 (electron, muon, tau) and a particle of charge 0 , which is the corresponding neutrino (electron neutrino, muon neutrino, tau neutrino). Each generation consists of two quarks with different charge: $+2/3$ and $-1/3$. The quarks are called *up* and *down* (first generation), *strange* and *charm* (second generation) and *bottom* and *top* for the third generation (see table 1.2).

Generation	1	2	3	Forces:
Quarks	u	c	t	γ
	d	s	b	g
Leptons	e	μ	τ	Z
	ν_e	ν_μ	ν_τ	W

Table 1.2: Fermions listed by their family and the force-carrying particles.

All particles interact via forces carried by exchange bosons: *gluons* for strong interactions in the theory of quantum chromo-dynamics, *photons* for electromagnetic forces,

W and Z bosons for weak interactions and the (hypothetical) *graviton* for the gravitation. These gauge bosons come up automatically in the theory of some fundamental symmetries. The electromagnetic and weak interactions are unified at higher energies. Therefore they are often combined and called *electroweak interactions*. Figure 1.3 shows how the theories melt together as energy increases.

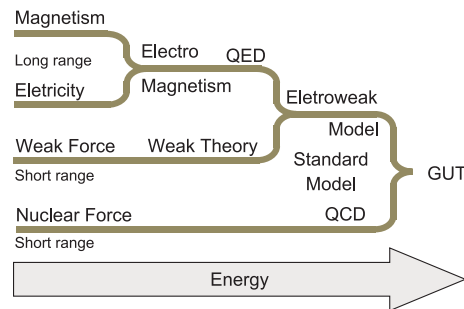


Figure 1.3: Unifications of theories at higher levels of energy. The energy is increasing from left to right in this diagram, leading to a *great unified theory* (GUT).

There is only one problem: All gauge bosons must have zero mass in the Standard Model. Experimental results have shown that this is true for photons and gluons, but not for the exchange particles of the weak interaction. Physicists have proven that the masses of the W and Z bosons are not null. Detailed measurements at particle accelerators around the world pointed out that the exact masses of W^- and Z -bosons are 80.4 GeV and 91.2 GeV, respectively. [4]. The remedy of this problem is to introduce a field called the *Higgs-Field* [6], which is not subjected to symmetry breaking. The W^- and Z -bosons acquire their mass by interacting with the vacuum Higgs field. This mechanism can also be used to explain the mass of the fermions. The existence of a Higgs field also implies its exchange particle: The Higgs-particle, which has not been experimentally verified yet. The Standard Model in its minimal version predicts a Higgs field doublet and a single neutral Higgs boson. Beyond this version, supersymmetric (SUSY) Higgs particles are considered, which are more compatible with existing high-precision data. The Minimal Supersymmetric Standard Model (MSSM) [7] is the SUSY extension of the Standard Model with fewest new particles. It needs two Higgs field doublets and predicts three neutral and two charged Higgs particles. While in the Standard Model the Higgs mass is not predicted, the MSSM predicts the mass of the neutral Higgs bosons close to the electroweak energy scale.

The search for and measurement of the exact masses of the Higgs bosons is one of the major goals of the LHC. ATLAS and CMS will have detectors optimized for Higgs boson search. The discovery will be possible between the full canonical mass range of 100 GeV to 1 TeV. This wide band is covered by a variety of production and decay processes. Figure 1.4 shows the integrated luminosity which is required for a discovery of the Standard Model Higgs boson. In the LHC startup, luminosity will be $0.12 \times 10^{34} \text{ cm}^{-2} \text{ s}^{-1}$, which gives an integrated luminosity of 30 fb^{-1} for the first year of operation. This makes a discovery of the Higgs boson likely.

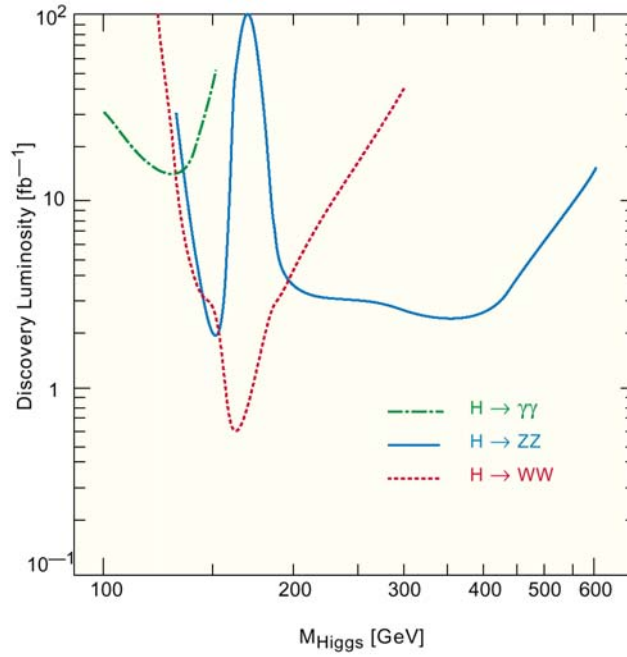


Figure 1.4: Integrated Luminosity required for the discovery (5σ signal-to-background ratio) of the Higgs as a function of the mass of the Higgs boson.

1.2.2 CP Violation

CP (*charge-parity*) violation plays an important role in cosmology. It could explain the excess of matter over antimatter observed in our universe [8]. Since the mechanism of CP violation in the weak interaction of the Standard Model is not enough to explain the dominance of matter, new sources have to be found. Its existence was discovered in 1964 [9] in the weak interactions of K mesons. In the B-meson system, many decay modes are possible, which will be studied at the LHCb experiment. B-mesons consist of a b - or anti- b -quark (\bar{b}) and a lighter Quark (d , s and their anti-particles):

$$\begin{aligned} B_d^0 &= \bar{b}d & \bar{B}_d^0 &= b\bar{d} \\ B_s^0 &= \bar{b}s & \bar{B}_s^0 &= b\bar{s} \end{aligned}$$

CP violation is generated by the complex 3×3 unitary matrix called Cabibbo-Kobayashi-Maskawa-matrix V_{CKM} [10], which describes the mixing of down-type quarks (d , s , b) to up-type quarks (u , c , t):

$$\begin{pmatrix} d' \\ s' \\ b' \end{pmatrix} = V_{CKM} \begin{pmatrix} d \\ s \\ b \end{pmatrix} = \begin{pmatrix} V_{ud} & V_{us} & V_{ub} \\ V_{cd} & V_{cs} & V_{cb} \\ V_{td} & V_{ts} & V_{tb} \end{pmatrix} \begin{pmatrix} d \\ s \\ b \end{pmatrix}$$

Six of the nine unitarity conditions of the CKM matrix can be drawn as triangles in the complex plane (see fig.1.5). The unitarity conditions are given by

$$V_{ud}V_{ub}^* + V_{cd}V_{cb}^* + V_{td}V_{tb}^* = 0$$

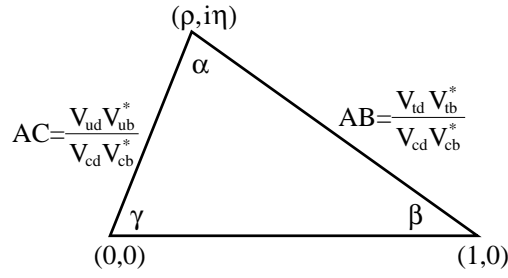


Figure 1.5: Unitarity triangle in the complex plane.

In the framework of the Standard Model, direct measurements of the angles α , β and γ can be made from CP asymmetries in different final states of B-meson decays. Well known decays are:

- $B_d^0 \rightarrow \pi\pi$ und $B_d^0 \rightarrow \rho\pi$ – angle α
- $B_d^0 \rightarrow J/\psi K_S^0$ – angle β
- $B_s^0 \rightarrow K_S^0 \rho^0$ and $B_s^0 \rightarrow D_s K$ – angle γ

Due to the high luminosity, the LHC will be a productive source of B-mesons at a high rate. About 10^{12} $b\bar{b}$ pairs are expected to be produced in one year of operation, which allows to make precise studies of CP asymmetry.

1.2.3 Quark-Gluon-Plasma

The LHC is designed to produce collisions of relativistic heavy ions (e.g. lead) as well. During such collisions, the very high density and temperature will cause a phase transition from 'ordinary' hadronic matter to a deconfined quark-gluon plasma, which may represent the conditions of the first seconds of our Universe. The ALICE experiment is designed to investigate this special phase of matter.

Chapter 2

The CMS Experiment

An experiment at LHC must have a very performant muon system to detect muon jets arising from proton-proton interactions [11]. The requirement of a compact design led to the choice of a strong magnetic field, which can only be produced by a superconducting solenoid. Thus the experiment is called *Compact Muon Solenoid* (CMS). It is planned to be a multi-purpose experiment with emphasis to the discovery of new physics, especially the Higgs boson and supersymmetric particles.

CMS can be divided into four large parts, which are shown in figure 2.1: the inner tracker, the electromagnetic and hadronic calorimeters and the muon system. These detector parts will be arranged like an onion in layers starting from the detector center which is the collision point. The central block is arranged in concentric cylinders around the beamline (*barrel*), covered by two *endcaps* perpendicular to the beamline. Table 2.1 gives an overview of the types of particles which can be detected by the different detector systems. This is also shown in figure 2.2, which illustrates the way of the particles through the CMS detector components.

	electrons	photons	pions	neutrons	muons
Tracker	✗		✗		✗
ECAL	✗	✗	✗		✗
HCAL			✗	✗	✗
Muon System					✗

Table 2.1: Types of particles which can be detected by the different detector systems of CMS. *ECAL* and *HCAL* stand for electromagnetic and hadronic calorimeters, respectively.

A longitudinal view of one quadrant of the experiment is shown in figure 2.3. The origin of r and z distances are in the center of the detector. The parameter η is called pseudorapidity as defined by

$$\eta = -\ln\left(\tan\frac{\alpha}{2}\right) \quad \text{and} \quad \frac{r}{z} = \tan\alpha, \quad (2.1)$$

where $\alpha = 90^\circ$ is perpendicular to and $\alpha = 0^\circ$ coincides with the beam axis.

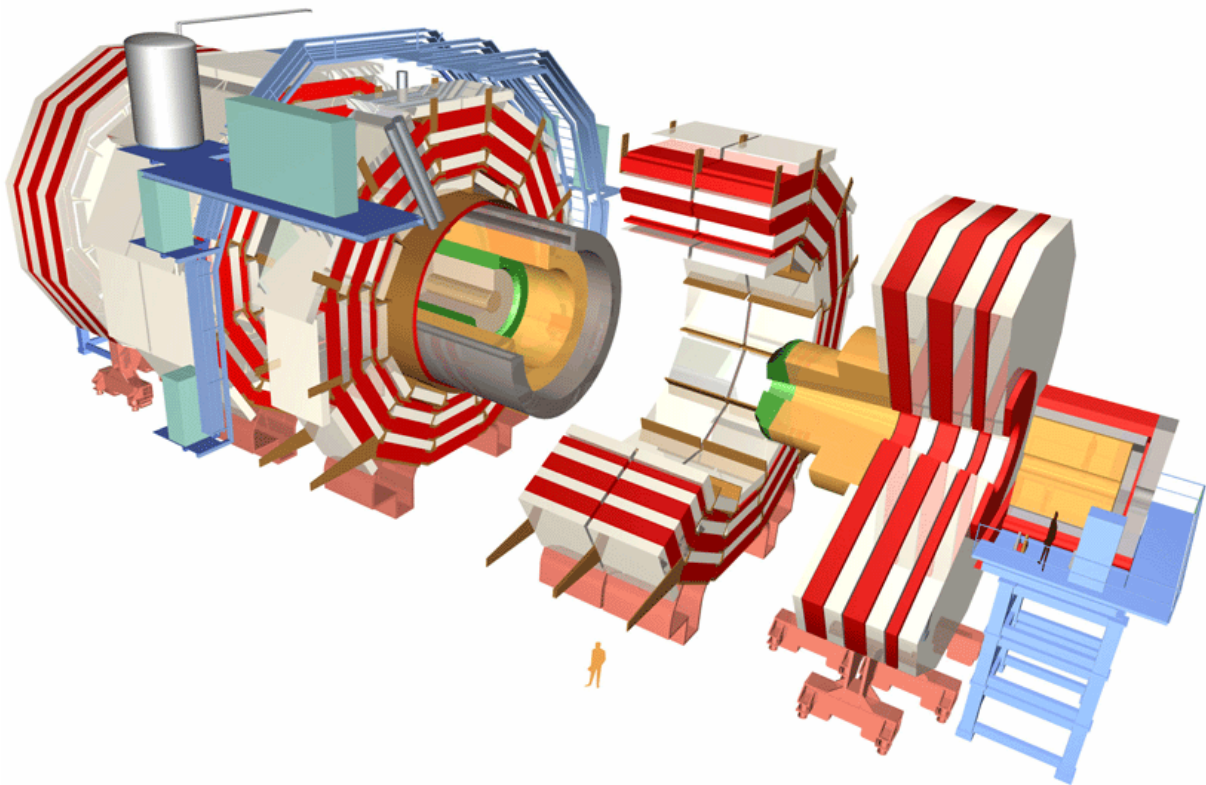


Figure 2.1: Three-dimensional Sketch of the CMS experiment. The tracking system is shown in pink and yellow, surrounded by the electromagnetic calorimeter (green) and the hadron calorimeter (purple). The muon detectors are drawn in yellow, while the iron yoke of the solenoid is shown in red.

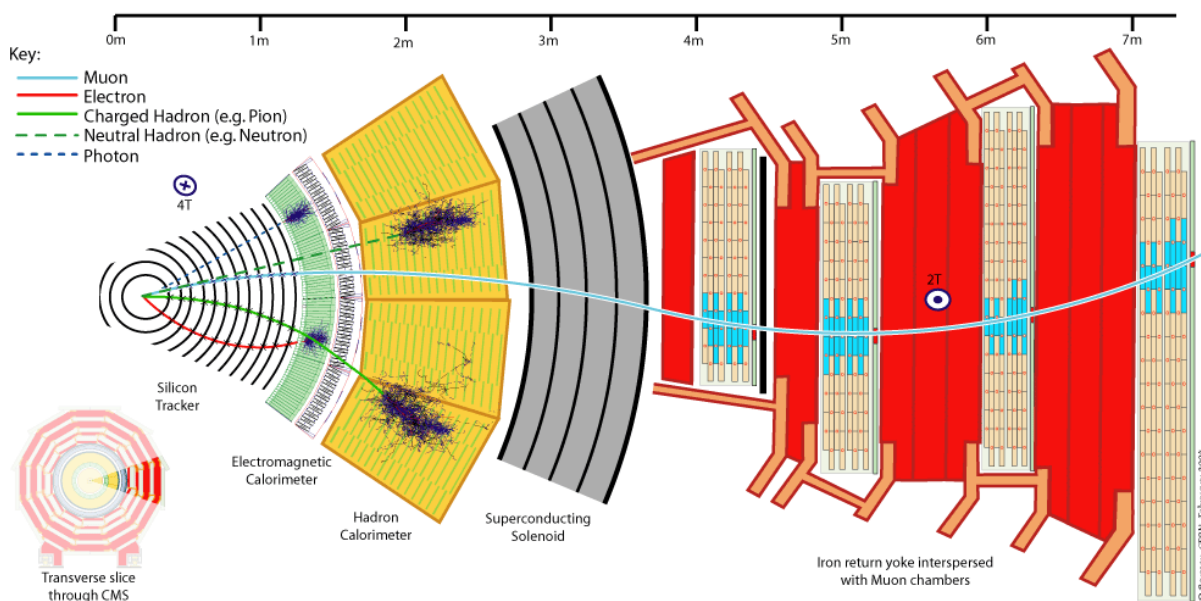


Figure 2.2: Illustration on how particles traverse the CMS experiment.

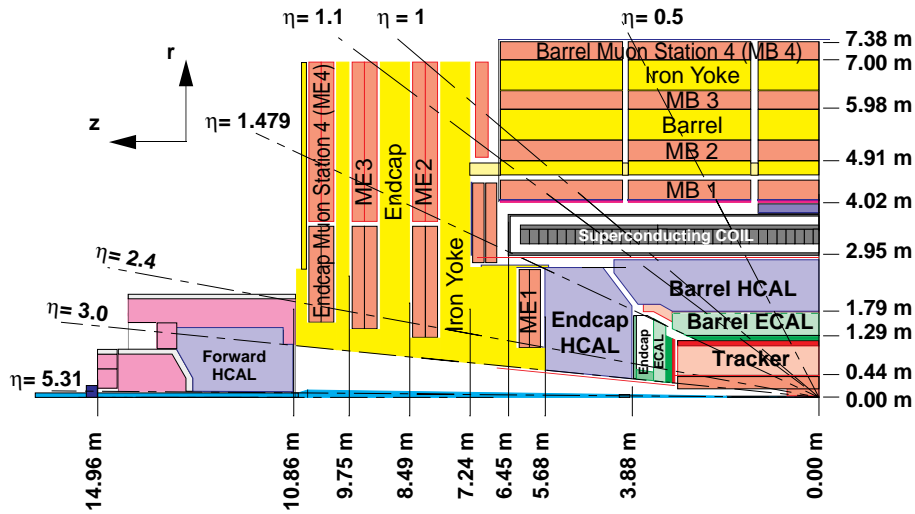


Figure 2.3: Longitudinal view of one quadrant of CMS.

2.1 The Superconducting Magnet

An uniform magnetic field of 4 T is required to achieve a good momentum resolution for high momentum muons [12]. This demands a superconducting magnet with a large diameter of 5.9 m and a length of 13 m. Because of these dimensions, the solenoid will contain both the tracker and the calorimetry. The magnetic flux is returned via three slices summing up to an 1.8 m thick saturated iron yoke which is instrumented with the muon detectors.

Many supporting systems, like cryogenics, power supply, vacuum pumps and quench protection are necessary for the superconducting coil. Quench protection is considered to be the most critical issue because of the enormous amount of stored energy. The protection is based on the "quench-back" effect already used in previous detector magnets [11]. The conductor itself consists of three concentric parts: the central superconducting Rutherford-cable made of NbTi stands, the aluminium stabiliser and the aluminium alloy insulation. The Rutherford-cable will have a cross-section of 693 mm², a total length of 43 km with 2112 turns and a nominal current of 20 kA. The cryogenic system is composed of internal and external parts. The internal system consists of two circuits, one liquid helium system for the winding and one for the thermal screen. The external system consists of a tank of 500 l liquid helium located near the solenoid, compressors and vessels for 200 m³ of pressurised He gas located at the surface level.

Since the magnet including the return yoke is the main element of CMS in terms of size and weight, it is used as the structural element to support all other barrel detector components.

2.2 Inner Tracker

The central tracker consists of three layers of silicon pixel and ten layers of silicon strip detectors (*sensors*). Initially, *Micro-Strip Gas Chambers* (MSGCs) were planned for its

outer part. However, problems were reported repeatedly concerning ageing and high voltage (HV) stability. Thus, the CMS Tracker collaboration decided to build an all-silicon tracker [13] instead, which now covers a sensitive area of 206 m^2 and will be the world largest silicon device.

The main task of a tracker is to quantify the momentum of a charged particle from its track in a magnetic field with a minimum of interaction. Because of the Lorentz force the trajectory of a particle with an electrical charge $e = \pm 1$ moving in a magnetic field B is a helix with curvature R . Its transverse momentum p_T with respect to the magnetic field is determined (non-relativistic) by:

$$p_T = eBR \quad (2.2)$$

Using position-sensitive devices like pixel (two-dimensional) and strip (one-dimensional) detectors in several layers around the interaction point, one can reconstruct the track of a charged particle through the tracker volume and calculate the transverse momentum. Moreover, the polarity can be obtained by the bend orientation.

Another important goal of the tracker is to reconstruct the vertex of a particle to determine its creation point. Particles escaping from the intersection point with very short lifetime decay after a very small distance of flight in the beampipe before reaching any tracking detectors. Identification of such particles is only possible via secondary vertices and requires high granularity of the detectors near the interaction point to distinguish neighbouring vertices.

The silicon pixel detector consists of three barrel and two endcap layers and is the innermost detector of CMS. Its main tasks are to assist in pattern recognition for the strip detector and to allow three-dimensional vertex reconstruction by providing a very high resolution, since one pixel cell has a size of only 0.02 mm^2 . The connection to the electronics is done via bump-bonding and demands a readout chip of the same size as the detector, which has to sustain the same harsh radiation level as the sensor.

The silicon strip sensors, as they are the main topic of this thesis, will be discussed in detail in later chapters.

2.3 Calorimetry

Calorimetry means to measure the energy of a particle by absorbing it completely. CMS utilizes both techniques, electromagnetic and hadronic calorimetry to be completely hermetic in terms of energy. This allows to identify also undetectable particles (e.g. neutrinos) by missing energy.

2.3.1 Electromagnetic Calorimeter

High energy electrons and photons interact with matter mainly through bremsstrahlung and pair production, respectively. Through these interactions,

secondary photons and electron-positron pairs are produced which interact in the same fashion, thus producing a cascade of charged and non-charged particles. This electromagnetic shower will stop when the energies of the created particles drop below a certain energy level. Below this level called critical energy ε , the multiplication process stops and the energy is dissipated by ionisation and excitation.

The quantity which describes the design of an ECAL is called *radiation length* X_0 . Within one radiation length an electron or photon loses $1/e$ of its energy. After n radiation lengths the growth of the shower will stop, since the energy has been degraded below the critical energy $E/e^n < \varepsilon$. The shower reaches its maximum after $n_{max} = \ln(E/\varepsilon)$ generations. The *Moliere radius* R_M describes the transversal dimension of such shower.

For CMS, lead tungstate (PbWO_4) has been chosen since it has good radiation hardness, a short radiation length and a small Moliere radius suitable to build a compact ECAL. The disadvantage of a low light yield is addressed by *Silicon Avalanche Photodiodes* (APDs). In total, 80,000 scintillation PbWO_4 crystals will be built, each connected to an APD or vacuum phototriode. A light-injection system has been developed for calibration.

2.3.2 Hadronic Calorimeter

The *hadron calorimeter* (HCAL) surrounds the electromagnetic calorimeter and measures the energy of hadronic particle jets, which also contain an electromagnetic component arising from π^0 production. Hadrons strongly interact with the nuclei in dense matter, creating hadronic showers, until the pion production threshold is reached.

Since a fully hermetic detector with 4π sensitivity is required to detect missing traverse energy, the HCAL design consists of a barrel and two endcap components and includes an additional *very forward calorimeter* which covers the pseudorapidity range between $3.0 < |\eta| < 5.0$.

Copper has been chosen as the absorption material to achieve a good *interaction length* λ , which is the equivalent to the radiation length of the ECAL. Moreover, a non-magnetic material is required to operate in the magnetic field of the solenoid without magnetic forces. Copper also has the advantage of low cost.

Plastic scintillators connected to wavelength shifters (WLS) are used to generate a light pulse. Together with the absorbing copper they build the sandwich-type HCAL. By optical fibres the green WLS light will be guided to the endcap region where the photodetectors are placed. APDs are used for this purpose as well as for the ECAL together with *proximity focussed hybrid photodiodes* (PFHPD).

2.4 Muon System

The outermost detector system is the muon system. It should fulfill three tasks: muon identification, trigger and momentum measurement. A wide coverage of pseudorapidity is required to allow an efficient detection. The barrel detector covers the region

$|\eta| < 1.3$, while the endcap detectors cover the region $0.9 < |\eta| < 2.4$ as shown in figure 2.3.

The muon detector is placed behind the calorimeters. It consists of four muon stations (MB1 to MB4 for the barrel, ME1 to ME4 for the endcap) interleaved with the iron return yoke plates leading to a sandwich shape. The identification is achieved by lining up the hits in at least two of the four muon stations. The magnetic flux in the iron provides an independent momentum measurement in addition to the tracker with a high reliability because of the four individual muon layers. The redundancy of the measurement makes the whole system robust against background.

In the barrel region, the muon stations are built of *drift tubes* (DTs), while *cathode strip chambers* (CSCs) are used in the endcaps. DTs can only operate in a rather uniform magnetic field, but the CSCs have to deal with a very intense and inhomogeneous magnetic field. *Resistive plate chambers* (RPC) are used in both barrel and endcap stations for fast trigger decisions.

DTs are gas-filled chambers made of aluminium tubes separated by conductive plates to build individual volumes in which thin wires are clamped. When an ionizing particle traverses the gas volume, electrons and ions are created which are collected by an electrical field between the tubes and the wires. Since the field is high around the wires, the ions and electrons ionize other gas molecules. This effect happens repeatedly so it is called avalanche gas amplification. The coordinate perpendicular to the wire is obtained from the drift time of the ionisation electrons to reach the wire, starting with the trigger signal of the fast RPC.

CSCs are also gaseous detectors. They work similarly as DTs but the cathodes are placed orthogonally below the wires, which yields a two-dimensional signal. The closely spaced wires make this device robust against strong and inhomogeneous magnetic fields as well as enabling a very fast readout. Each muon station consists of six CSCs.

Because of its fast response time of approximately 1 ns, *resistive plate chambers* (RPC) are used for bunch crossing identification and trigger. RPCs are parallel plate counters with two electrodes made of very high resistive plastic material. This allows very large and thin detectors operating at a very high rate. The small volume is filled with a gas mixture with a pickup plane segmented in strips in the centre between two chambers to measure the signal from both gas volumes.

Chapter 3

The CMS Silicon Strip Sensors and their Qualification Procedure

As mentioned in the previous chapter, the CMS barrel tracker consists of three layers of silicon pixel detectors in the innermost region surrounded by ten layers of silicon strip sensors. In the endcaps, it consists of two pixel layers and nine strip disks, altogether covering a pseudorapidity of $|\eta| \leq 2.5$. The tracking system will play a major role for CMS operation, especially performing efficient track finding. It has to cope with high radiation levels and particle fluxes and needs to have a high granularity and good spatial precision of down to $20 \mu m$ in the transverse plane and $100 \mu m$ in z direction.

3.1 Energy Loss

Particles traversing a solid state detector device lose energy since free electron-hole pairs are generated. These free charges move towards opposite electrodes under the influence of an electric field. The energy loss of moderately relativistic charged particles in matter was first described by H.A. Bethe and F. Bloch using equation 3.1 [4].

$$-\frac{dE}{dx} = C_0 z^2 \frac{Z}{A} \frac{1}{\beta^2} \left[\frac{1}{2} \ln \left(\frac{2m_e c^2 \beta^2 \gamma^2 T_{\max}}{I^2} \right) - \beta^2 - \frac{\delta(\gamma)}{2} - \frac{C}{Z} \right] \quad (3.1)$$

It represents the differential energy loss per mass surface density in units of $[\text{MeV}/(\text{g cm}^{-2})]$. The used symbols denote

C_0	=	$4\pi\rho N_A r_e^2 m_e c^2$
ze	...	charge of the incident particle
N_A	...	Avogadro's number
Z	...	atomic number
A	...	atomic mass of the material
m_e	...	electron mass
r_e	=	$\frac{e^2}{4\pi\epsilon_0 m_e c^2}$ (classical electron radius)
T_{max}	...	maximum kinetic energy which can be imparted to a free electron in a single collision
I	...	mean excitation energy $[eV]$
$\delta(\gamma)$...	density effect correction to ionization energy loss
C	...	shell correction term
β	=	v/c
γ	=	$(1 - \beta^2)^{-1/2}$

In thin layers like semiconductor detectors (typical thickness of 300-500 μm) the deposited energy is less than expected because a fraction of the energy is carried off by high energetic δ electrons. These considerations lead to the restricted energy loss, which is expressed by an additional term in the Bethe-Bloch equation [14],

$$-\frac{dE}{dx} = C_0 z^2 \frac{Z}{A} \frac{1}{\beta^2} \left[\frac{1}{2} \ln \left(\frac{2m_e c^2 \beta^2 \gamma^2 T_{\text{upper}}}{I^2} \right) - \beta^2 \left(1 + \frac{T_{\text{upper}}}{T_{\text{max}}} \right) - \frac{\delta(\gamma)}{2} - \frac{C}{Z} \right] \quad (3.2)$$

where

$$T_{\text{upper}} = \min(T_{\text{cut}}, T_{\text{max}}) \quad (3.3)$$

with T_{cut} depending on the material and the incident particle momentum. Figure 3.1 shows a comparison of the standard Bethe-Bloch equation to the restricted form for a pion traversing 300 μm of silicon. No difference can be seen for particles below 50 MeV. For higher energies, the relativistic rise is quite flat in the restricted model due to the energy taken away by δ electrons. Figure 3.2 shows the energy loss rate for different particles and mediums.

3.2 Charge Collection

The energy deposited in the detector material leads to the creation of free electron-hole pairs as shown in figure 3.3. If an electrical field is present between two electrodes the electrons and holes are drawn off the detector. The speed of their movement is known as carrier drift velocity v which is proportional to the electric field up to a saturation level. The proportional constant is called carrier mobility μ and is $\mu_n = 1450 \text{ cm}^2/\text{Vs}$ for electrons and $\mu_p = 450 \text{ cm}^2/\text{Vs}$ for holes, respectively [4].

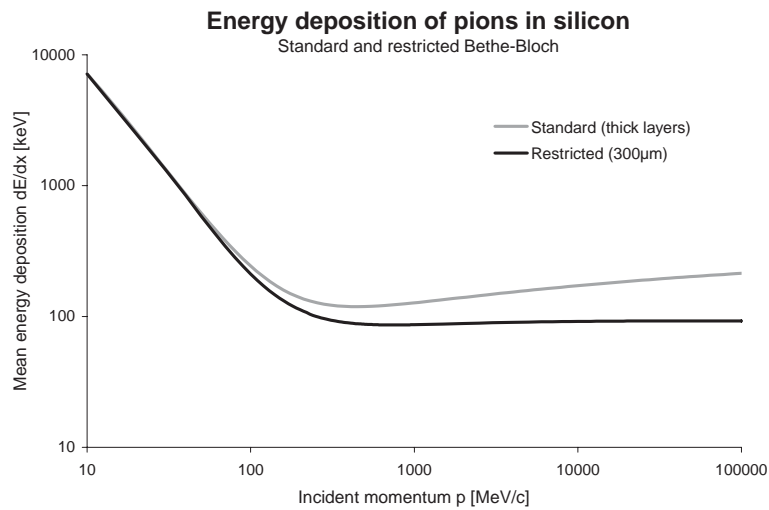


Figure 3.1: Comparison of the standard Bethe-Bloch equation to the restricted form for a pion traversing 300 μ m of silicon [15].

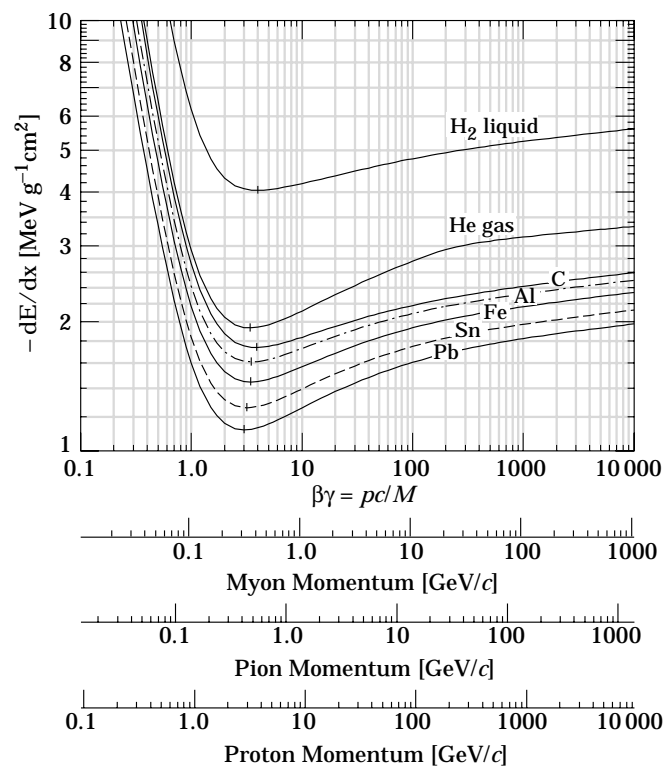


Figure 3.2: Energy loss for different particles and mediums [4].

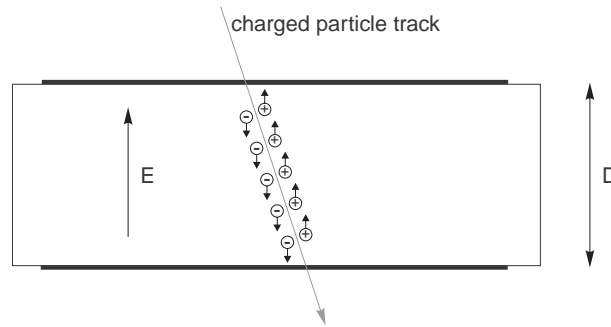


Figure 3.3: A charged particle traversing the detector generates free electron-hole pairs along its track. In the presence of an electrical field E the charges are drained by the electrodes.

The number n of created charges is the quotient of the total energy loss E_{loss} of the incident particle and the energy necessary for pair production (ionization energy E_{eh}),

$$n = \frac{E_{\text{loss}}}{E_{eh}} . \quad (3.4)$$

In silicon, $E_{eh} = 3.6 \text{ eV}$, which results in a most probable charge of about $n = 22500$ pairs for a *minmum ionizing particle* (MIP) in a standard silicon detector of $300 \mu\text{m}$ thickness. The measured energy loss distribution of MIPs is shown in fig. 3.4 for such a detector in terms of the collected charge [15]. The shape of the curve is a convolution

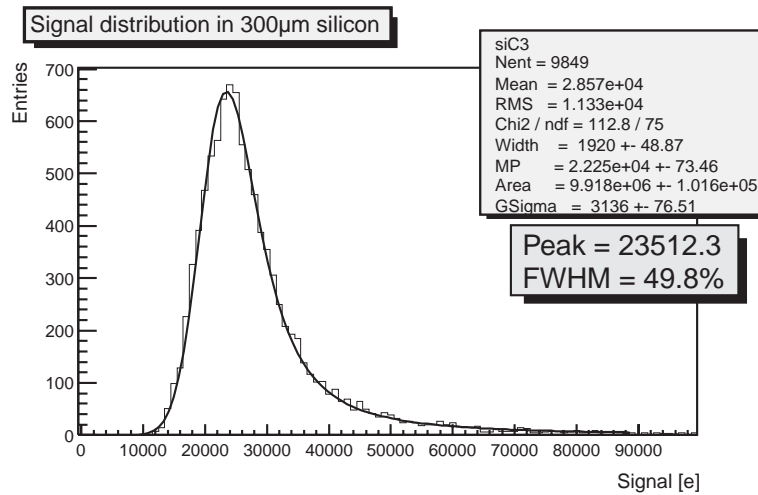


Figure 3.4: Measured MIP signal distribution in a silicon detector of a thickness of $300 \mu\text{m}$.

of a Gauss with a *Landau distribution* [16]. The long upper tail is called *Landau tail* and is due to rare, but highly energetic δ electrons and extends to infinite energies in theory, which also implies a infinite mean value. In contrast to its mathematical properties the

measured mean energy loss is not identical with the *most probable* (MP) as a result of its asymmetry. The MP represents the peak of the distribution and is typically lower than the mean value by a factor of about 1.2 – 1.3.

A charge moving inside the detector bulk induces a current, independently of whether the carriers eventually reach the electrodes or not. This current j is proportional to the sum of both carrier velocities [17],

$$j = \frac{e}{D} \left(\sum v_e + \sum v_h \right) \quad (3.5)$$

with the elementary charge e , the detector thickness D and the carrier drift velocities v_e and v_p for electrons and holes, respectively. The integrated current gives the total collected charge Q_c , which can be measured by integrating amplifiers,

$$Q_c = \frac{e}{D} \int \left(\sum v_e + \sum v_h \right) dt \quad . \quad (3.6)$$

3.3 Silicon Sensor Characteristics

In a standard silicon sensor the total number of free charge carriers in intrinsic silicon is four orders of magnitude higher than the number of electron-hole pairs created by a MIP. The *signal-to-noise ratio* (SNR) for such a scenario is quite low. Thus the intrinsic carrier density must be reduced, which is achieved by depleting the detector of free carriers through a reversely biased diode. Two semiconductor materials of p and n types doped with impurity concentration of acceptors N_a and donors N_d brought together forming an abrupt transition, called $p - n$ *junction*. Because of a gradient of electron and hole densities a diffusive migration of majority carriers occurs across the junction leading to a region called *space charge* or *depletion region*, where no free carriers exist [18]. The migration sets up a barrier to further migration, which is self-adjusted in the equilibrium state. The potential and electric field distributions can be calculated using the one-dimensional Poisson equation

$$\frac{\partial^2 \varphi}{\partial x^2} = -\frac{\rho}{\varepsilon} \quad . \quad (3.7)$$

where φ is the potential and ε denotes the dielectric constant. The space charge density in the p and n regions is $-eN_a$ and eN_d respectively. Since the volume is neutral, the widths of the depletion layer on the p - and n -sides – W_p and W_n – obey the condition

$$N_a \cdot W_a = N_d \cdot W_d \quad (3.8)$$

Integrating the Poisson equation 3.7 twice, the potential barriers on both sides of the junction yield

$$\varphi_a = \frac{eN_a W_a^2}{2\varepsilon} \quad (3.9)$$

$$\varphi_d = \frac{eN_d W_d^2}{2\varepsilon} \quad (3.10)$$

A typical silicon detector is based on n-type bulk material in which a pn -junction is introduced near the surface by heavily doping with acceptors, resulting in zones of p^+ types. Once the junction is under reverse bias voltage, all free carriers in the bulk are drained by the electric field. The opposite side is known as backplane. The backplane is metallized to get a good ohmic contact, which is improved by the n^+ -type implant beneath the metallization. The thicknesses of the p^+ - and n^+ -type implants are in the order of a micrometer, such that the difference between bulk and total detector thickness is negligible. The profile of a typical silicon detector is shown in figure 3.5.

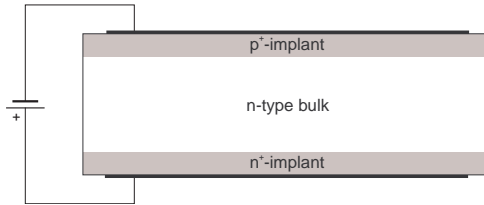


Figure 3.5: Schematic profile of a silicon detector. The implants are shown at enlarged scale.

Combining the above equations, the depletion voltage of such a sensor is

$$V_{\text{Depl}} = \frac{e N_{\text{bulk}} W^2}{2\epsilon} \quad (3.11)$$

where $W = W_d + W_a$ is the total depletion depth and $N_{\text{bulk}} = N_a$.

In silicon sensors, the depletion region is free of charge carriers, but electron-hole pairs are thermally generated continuously everywhere within the volume. Without an electric field, the created carriers recombine. However, an electric field separates electrons and holes immediately after generation, leaving them little chance to recombine.

The total current J_{tot} in a reverse-biased silicon detector is the sum of the thermal current in the depleted region J_{th} and the diffusion current of the pn -junction J_{diff} .

$$J_{\text{tot}} = J_{\text{th}} + J_{\text{diff}} \quad (3.12)$$

The thermal current can be expressed [19] as

$$J_{\text{th}} = \frac{n_i e}{\tau_g} \cdot W \quad (3.13)$$

using the intrinsic carrier density $n_i = 1.45 \times 10^{10} \text{ cm}^{-3}$ at room temperature, the depletion layer depth W and the generation lifetime of the majority charge carriers τ_g . This lifetime was measured to be $4300 \mu\text{s} < \tau_g < 6500 \mu\text{s}$ [20]. The thermal current component is proportional to the width of the depletion zone W and thus scales with $\sqrt{V_{\text{bias}}}$.

The second fraction of the total current, the diffusion current, can be calculated using

$$J_{\text{diff}} = \left(\frac{e D_n n_{p0}}{L_n} + \frac{e D_p p_{n0}}{L_p} \right) \left(e^{\frac{eV}{k_B T}} - 1 \right) \quad (3.14)$$

where k_B is the Boltzmann constant, L_n and L_p are the diffusion lengths and D_n and D_p are the diffusion constants of the electrons and the holes, respectively. The diffusion length can be derived from its relation to the lifetime, which is $L_n = \sqrt{D_n \cdot \tau_n}$ and similar for holes. The diffusion constants can be calculated using Einstein's relation $D_n = \mu_n \cdot \frac{k_B T}{e}$ for electrons and analogous for holes. The parameters n_{p0} and p_{n0} are the equilibrium densities of the minority charge carriers in the p and n type materials, respectively. Their values can be derived from

$$n_i^2 = n_{p0} \cdot p_{p0} \quad (3.15)$$

which leads to

$$n_{p0} = \frac{n_i^2}{N_A - N_D} \quad (3.16)$$

for holes and analogous for electrons.

The total leakage current in silicon detectors is temperature dependent according to

$$J \propto T^2 e^{-\frac{E_g}{2k_B T}}, \quad (3.17)$$

where T is the operating temperature and $E_g = 1.1$ eV the band gap. According to eq. 3.17, there is a factor of approximately 15 between the leakage currents at room temperature and the temperature of -10° C.

3.4 Radiation Damage

The total flux of photons, neutrons and charged hadrons expected in the CMS experiment is very high. In the region of the tracker, charged hadrons are dominant, which are mostly pions with a momentum below 1 GeV/c. The expected radiation fluences of photons, neutrons and charged hadrons are shown in fig. 3.6.

One effect of the irradiation of n-doped semiconductor devices is the removal of donors and the generation of acceptor-like defects. This effect reduces the effective bulk doping concentration

$$N_{\text{bulk}} = |N_D - N_A| \quad (3.18)$$

until the doping concentration is zero and the device behaves like an intrinsic semiconductor. This state is called *inversion point*. With further irradiation, acceptors dominate and the bulk material acts like a p -type semiconductor. This effect is called *type inversion*. As the depletion voltage scales with the bulk doping concentration, the bias voltage has to be adjusted during the irradiation to ensure a full depletion. Initially the depletion voltage decreases until it theoretically reaches zero in the inversion point. After that, the depletion voltage rises proportionally to the fluence. The level of fluence needed for type inversion depends on the initial number of donors. High resistivity sensors have a low initial donor density and reach the inversion point with less fluence than sensors with low resistivity.

With irradiation, also defects are introduced in the silicon bulk material which act as charge traps and recombination centers. This leads to a reduction of the *charge collection*

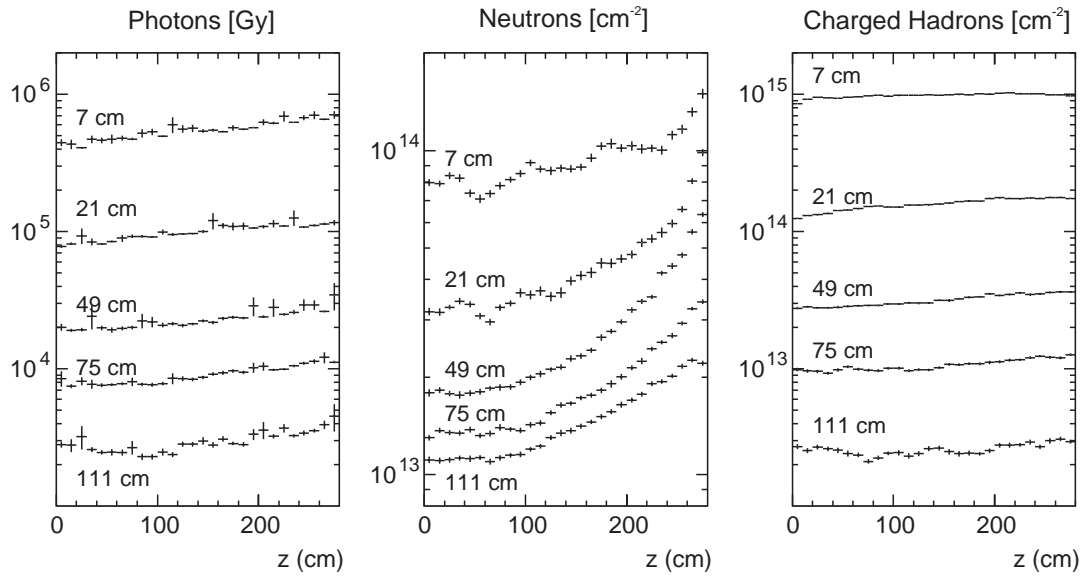


Figure 3.6: The expected fluences of photons, neutrons and charged hadrons in the CMS experiment over 10 years of operation as a function of the longitudinal distance z and the radius r .

efficiency. The probability of charge trapping is proportional to the drift time. Thus a higher bias voltage has to be applied which results in shorter drift times to compensate this effect.

Moreover, radiation damage causes an increase of the detector leakage current J_{leak} , which is proportional to the equivalent fluence Φ_{eq} and the sensitive volume V ,

$$\Delta J_{\text{leak}} = \alpha \Phi_{\text{eq}} V \quad (3.19)$$

where α is the material independent *current related damage rate*. At room temperature, values between 4 and $10 \cdot 10^{-17}$ A/cm are given in literature. This parameter scales with the temperature as the current does (eq. 3.17) and thus is reduced approximately by a factor of 15 for the operating temperature of -10° C.

3.5 Tracker Geometry

The CMS barrel tracker is composed of ten layers of silicon strip sensors. In the end-caps, it consists of nine disks, altogether covering a pseudorapidity of $|\eta| \leq 2.5$. The layout of the tracker is shown in figure 3.7. The four *inner barrel* layers (TIB) are assembled concentrically around the beampipe and are complemented by an *inner disk* (TID) on each side, which is built of three rings on three disks. The *outer barrel* (TOB) consists of six concentric layers. It is covered by the two *endcaps* (TEC), in which seven rings on nine disks are mounted. Each disk consists of 16 sectors called petals. The complete tracker will operate at a temperature of -10° C in a dry atmosphere of below 30 % relative humidity.

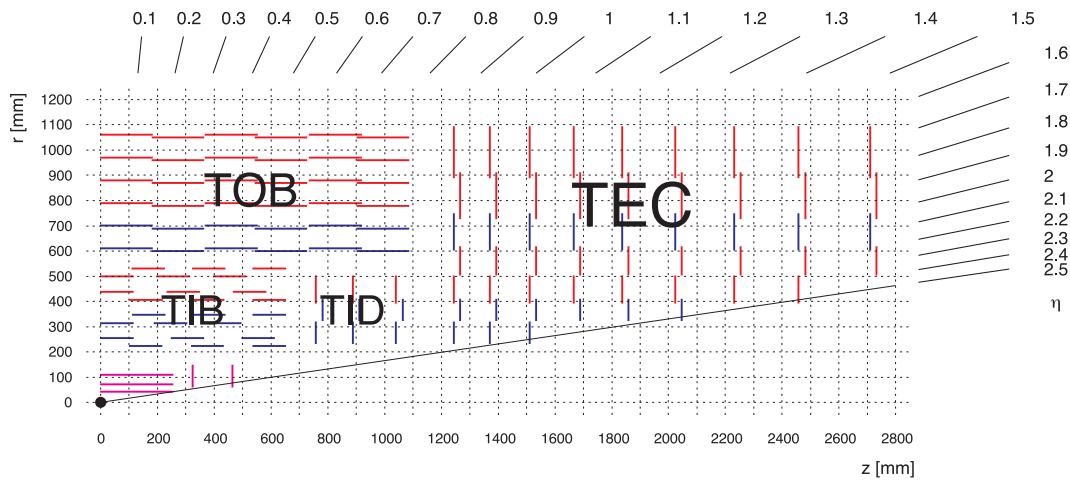


Figure 3.7: One quadrant of the CMS Tracker. Pixel detector layers are shown in pink, while strip detectors are in red (single-sided) and blue (double-sided). The tracker consists of the *tracker inner barrel* (TIB), the *tracker inner disk* (TID), the *tracker outer barrel* (TOB) and the *tracker endcaps* (TEC).

The basic detection unit of the tracker is called *module* and is built up by a supporting structure called *frame* onto which one or two silicon sensors are glued together with the front end hybrid. Modules mounted in the *inner region* (TIB, TID and the first four rings of TEC) consist of one silicon sensor, while in modules of the *outer regions* (TOB and ring 5-7 of TEC) two sensors are daisy-chained together. The main element of the front end hybrid is the readout chip called APV25. One single readout chip connects to 128 individual strips of the silicon sensor. Thus, four and six APVs are needed to read out sensors with 512 and 768 strips, respectively. The connection to the sensors is made via wire-bonding and a space-changing *pitch adapter*. The modules shown in figure 3.7 in blue are double-sided modules, which are made of two single sided modules mounted back-to-back under an angle of 100 mrad (5.7°).

3.6 Sensor Design

Two different sensors types are used to achieve a stable operation under the harsh radiation of the $p - p$ interactions [21]. Sensors mounted on modules in the inner region of the tracker are *thin* sensors with a thickness of $320 \mu\text{m}$ and a *low* resistivity ($1.5 - 3 \text{ k}\Omega \text{ cm}$) and are produced by the Japanese company *Hamamatsu Photonics K.K.* (HPK) [22]. Sensors of the outer region are delivered by the Italian *STMicroelectronics* (STM) [23] company with an thickness of $500 \mu\text{m}$ and a *high* resistivity ($3.5\text{-}7.5 \text{ k}\Omega \text{ cm}$). 15 different geometries of sensors are foreseen in the CMS tracker: Two rectangular types for the TIB, two for TOB and 11 wedge-shaped sensors for TID and TEC. The geometrical dimensions, the strip pitch, the number of strips per sensor and the total number of required sensors are shown in table 3.1 [24].

Each single sensor is produced on one silicon wafer which has a special lattice orientation of $\langle 100 \rangle$ which was demonstrated to be superior to $\langle 111 \rangle$ in terms of radiation

type	length [mm]	height [mm]	pitch [μm]	strips	quantity
IB1	63.3	119.0	80	768	1536
IB2	63.3	119.0	120	512	1188
OB1	96.4	94.4	122	768	3360
OB2	96.4	94.4	183	512	7056
W1 TEC	64.1-87.9	87.2	81-112	768	288
W1 TID	63.6-93.8	112.9	80.5-119	768	288
W2	88.1-112.2	90.2	113-143	768	864
W3	64.9-83.0	112.7	123-158	512	880
W4	59.7-73.2	117.2	113-139	512	1008
W5a	98.9-112.3	84.0	126-142	768	1440
W5b	112.5-122.8	66.0	143-156	768	1440
W6a	86.1-97.4	99.0	163-185	512	1008
W6b	97.5-107.5	87.8	185-205	512	1008
W7a	74.0-82.9	109.8	140-156	512	1440
W7b	82.9-90.8	98.8	156-172	512	1440

Table 3.1: Geometrical dimensions of the strip sensors. The thin sensors of the inner barrel (IB) and the thick sensors of the outer barrel (OB) are rectangular. The sensors of the endcaps (TEC) are wedge-shaped (W1-W7).

hardness [25]. Its thickness has to be within $20 \mu\text{m}$ of the specification. The tolerance of the mask alignment must be better than $1 \mu\text{m}$.

p^+ implants are placed on the front side of the detector to define 512 or 768 strips depending on the sensor geometry. A width-over-strip ratio of 0.25 is used for the strip implants for all geometries. Above the p^+ strips an oxide insulation layer of silicon oxide and silicon nitride is accumulated. An aluminium layer on the top of the oxide but 15 % wider than the implant, allows an AC coupled readout. This metal overhang changes the electrical field and makes the sensor more resistant against electrical breakdown by avoiding high field gradients. The implanted strips are connected to a probing pad named *DC pad* while the aluminium strip is connected to the *AC pad*. Each implanted strip is connected to the bias line by a polysilicon resistor, which is used to apply the bias voltage. A guard ring is placed around the bias line which also utilizes the metal overhang technique. This avoids breakdowns while operating at high voltages. A n^+ implant is required on the backside to provide a good ohmic contact to the *backplane* metallization. A sketch of a detector profile is shown in figure 3.8.

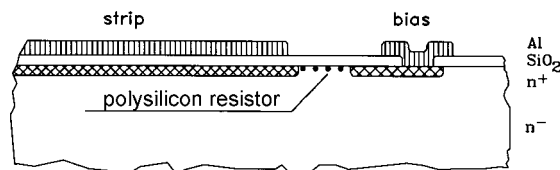


Figure 3.8: Profile of a typical silicon strip detector with AC coupled readout.

Both thin and thick sensor types are manufactured in the standard planar photolithographic process employed by industry. One single detector can be placed within the fiducial circle of about 13.5 cm of a 6" wafer. Four additional devices called *teststructures* surround the sensor. These devices are semicircle-shaped and thus are called *half moons*. One of the four teststructures was designed by the tracker collaboration with an identical layout for both vendors. It consists of nine sub-structures (see fig. 4.1) allowing measurements to monitor the stability of the production process.

3.7 The Sensor Quality Assurance

The large number of sensors required for the CMS tracker requires a sophisticated quality assurance procedure to ensure stable parameters within the production time and to verify the full compliance of all sensors with the technical specifications [26]. Thus, various measurements have been developed to achieve these requirements [24], which should be passed by at least 98 % of the delivered sensors.

The logistics and workflow of this procedure is shown in figure 3.9. The sensors are

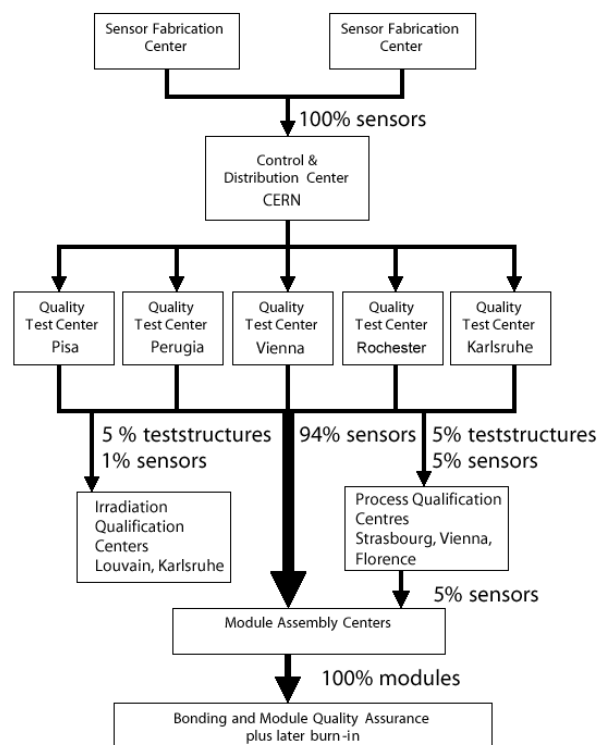


Figure 3.9: Sensor Logistics and flow within the involved labs and tests.

shipped from both companies to CERN where they are registered, which means that their *OBJECT_ID* (a 14 digit unique number for each sensor) is entered into the tracker construction database (see next section). After that, the sensors and the corresponding teststructures are shipped to the *Quality Test Centers* (QTC) located in Pisa, Perugia, Vienna, Rochester and Karlsruhe, where samples of sensors are fully characterized. This

means that IV and CV curves are recorded and four different parameters are measured on each single strip: the single strip current (I_{strip}), the polysilicon resistance (R_{poly}), the coupling capacity (C_{ac}) and the dielectric current (I_{diel}). A small percentage of the sensors and teststructures are sent to the *Process Quality Control* (PQC) centers, which are also responsible for the *Longterm Validation* (LTV), where sensor dark current stability tests are performed. Another small sample of sensors and teststructures will be distributed to *Irradiation Qualification Centers* (IQC) where they are irradiated with neutrons and protons. A further small percentage of the teststructures will be sent to the bonding centers, where pulltests are performed to check the adhesion of wire bonds. After qualifying a full batch, the accepted sensors are finally forwarded to the *Module Assembly Centers*, where the sensors will be assembled into Modules and further tests take place on module level.

HEPHY Vienna acts as QTC, PQC and LTV center as well as a module assembly center.

3.8 The Tracker Database

The large number of tests and measurements require an efficient data storage and traceability of the objects. Thus, a central relational database system was established at CNRS Lyon using Oracle [27] (*TrackerDB*). Every single measurement result has to be written in a data file using XML format and is uploaded to the TrackerDB, which enables a rational extraction of data for statistics and analysis. All PQC and LTV measurement data done in the context of this thesis were uploaded to TrackerDB. The plots shown in the end of chapters 4 and 5 are created by extracting data using a self written *Relay Application* [28] and *VisualDB* [29].

Chapter 4

Process Quality Control

As mentioned earlier, each wafer hosts additional devices beyond the sensor, designed to monitor the stability of the manufacturing process. Since the test structure was processed on the same wafer as the sensor, we can assume that both perform identical or exhibit the same weaknesses.

A standard set of nine structures, requested by the Tracker Collaboration, is placed inside the fiducial region (*standard half-moon*) as shown in Fig.4.1. The PQC test centres at INFN Florence [30], IReS Strasbourg [31] and HEPHY Vienna are responsible for the measurement of them.

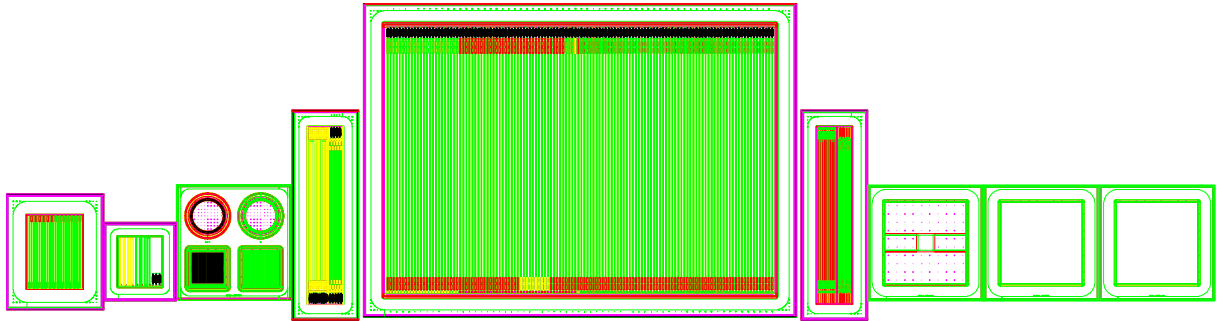


Figure 4.1: View of the Standard half-moon. The devices are (from left to right): TS-CAP, sheet, GCD, CAP-TS-AC, baby, CAP-TS-DC, diode, MOS1 and MOS2.

4.1 Measurement Setup

The PQC setup in Vienna is based on a probecard contacting all needed pads of the teststructure with a set of 50 needles. The probecard was supplied by an industrial manufacturer [32]. A schematic overview of the setup is shown in fig. 4.2. The measurement itself is performed in a light-tight box, monitoring its environmental conditions (temperature and relative humidity) by a TRHX system [33]. A computer is connected to the instruments via the *General Purpose Interface Bus* (GPIB) [34] for control and data

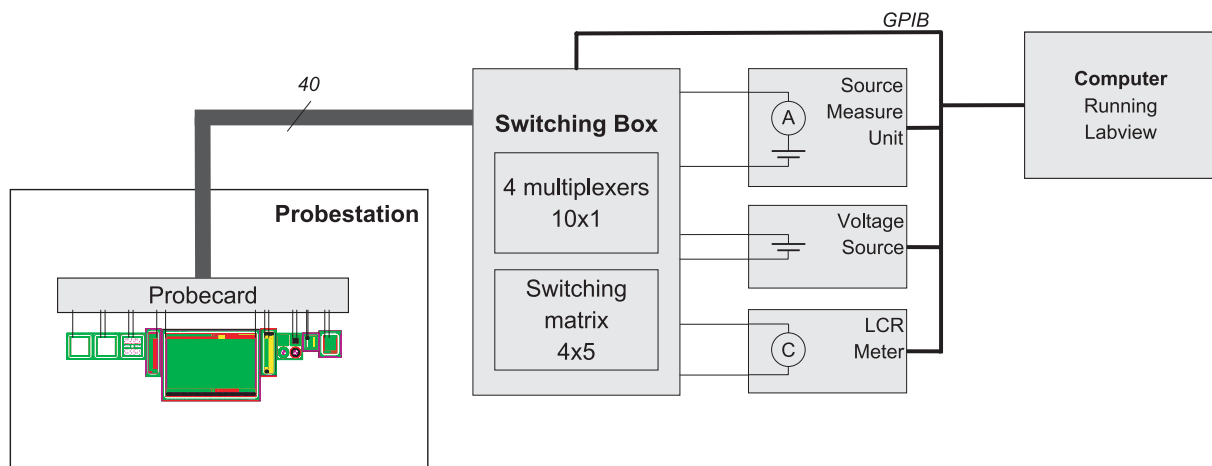


Figure 4.2: Schematics of the PQC setup with the connected instruments.

retrieval. A barcode scanner allows an easy way to read the OBJECT_ID of the test-structure into the computer.

Each needle is connected to an input channel of four Keithley 7154 multiplexer cards (10×1 contacts) plugged into a Keithley 7002 switching frame. The multiplexer outputs are interfaced through a Keithley 7153 5×4 matrix card (which is also part of the switching frame) to the following instruments:

HV source measure unit (Keithley 237): Very precise *source measure unit* (SMU).

V source (Keithley 595 or Keithley 2410): Additional voltage source required for some of the measurements.

LCR meter (Agilent HP4285A): Capacitance measurement instrument using high frequency between 75 kHz and 30 MHz. In our measurements, we use a signal level of 100 mV. This instrument has an upstream decoupling box to allow a DC bias voltage beyond the instrument's limit of 40 V.

A photo of the probecard and the multiplexer cards is shown in figure 4.3. The detailed scheme of the connections of the switching system (fig. A.1) and a table with the allocation between the pins of the connector and the probecard and the contact names (table A.1) are given in the appendix.

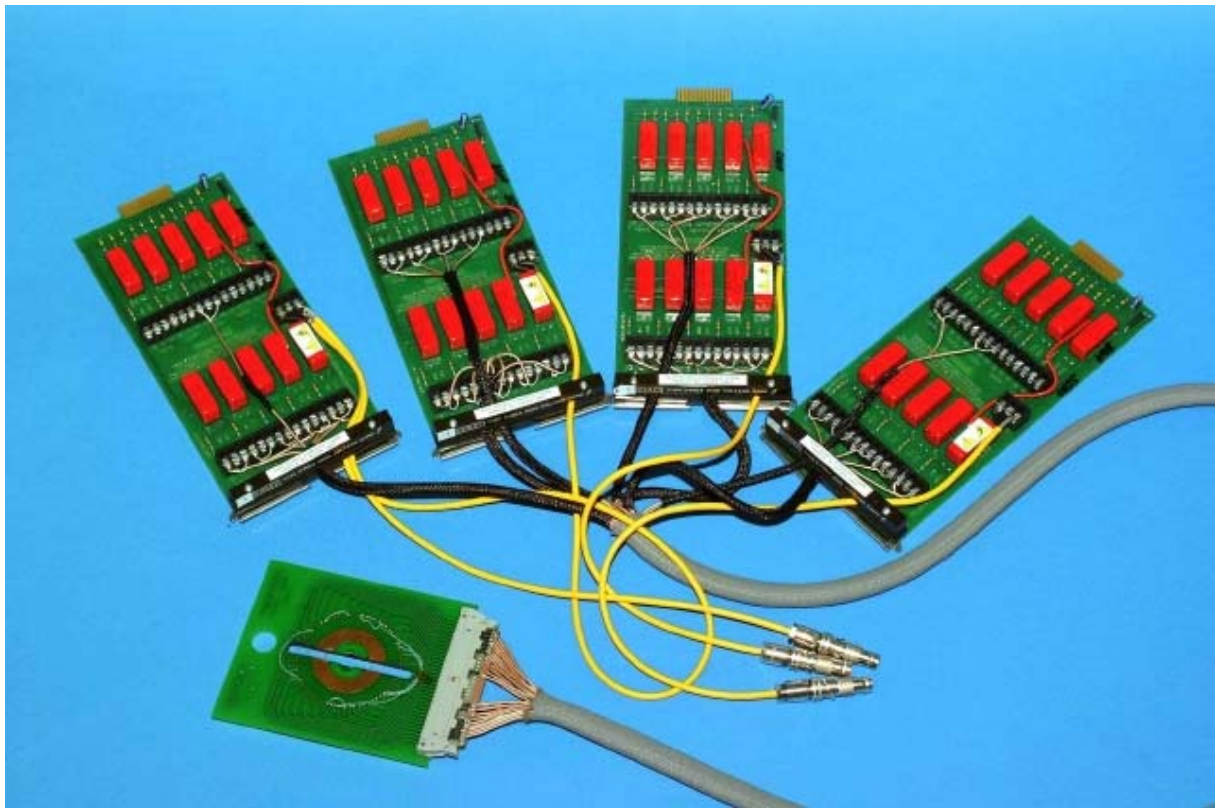


Figure 4.3: Picture of the probecard connected to the four K7154 multiplexer cards. The yellow cables are connected to the K7153 matrix card.

4.2 Description of Measurements

4.2.1 Coupling Capacitance (C_{ac})

The structure *TS-CAP* is an array of 26 strips (see fig. 4.4) connected directly to the bias ring without any polysilicon resistor. Each strip can be read out by its AC pad that is placed alternatively on the two opposite ends of the strips. The dielectric structure is the same as for the main detector:

- a layer of SiO_2
- a thin layer of Si_3N_4

For STM we assume a thickness of 2000 Å for the SiO_2 layer [35] and a 700 Å thick Si_3N_4 layer. For HPK the thicknesses are not known.

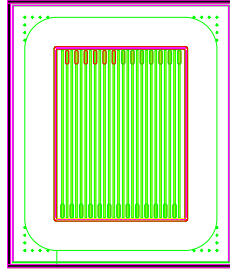


Figure 4.4: Layout of C_{ac} structure.

The probecard connects to six of the strips (number 3, 7, 11, 15, 19, 23) for which the AC pads are all placed at the bottom side of the structure. The quality of the dielectric is analysed with this device. This is done by the capacitance and the dielectric breakdown voltage measurements, respectively.

The CMS specifications of the coupling capacitance are $C_{ac} > 1.2 \text{ pF cm}^{-1} \mu\text{m}^{-1}$ per implanted strip width. For this structure, we find a capacitance for one strip of

$$1.2 \text{ pF cm}^{-1} \mu\text{m}^{-1} \times \underbrace{4.413 \text{ mm}}_{\text{strip length}} \times \underbrace{30 \mu\text{m}}_{\text{strip width}} = 15.89 \text{ pF}. \quad (4.1)$$

In order to extract the 6 values of C_{ac} it is important to subtract the stray capacitance of the system. This parameter is measured for each channel in open mode and the values are shown in table 4.2.1.

The thickness of the oxide layer is derived from the common parallel plate capacitor equation (see equation 4.2).

$$C = \varepsilon_0 \varepsilon_r \frac{A}{d} \quad (4.2)$$

However, our oxide layer is composed of two oxides, which can be described by two capacitors connected in series. The total capacitance of such a system is defined by

$$C_{\text{tot}} = 1 / \left(\frac{1}{C_1} + \frac{1}{C_2} \right) = \frac{C_1 \cdot C_2}{C_1 + C_2} \quad (4.3)$$

strip	C [pF]
cc1	2.38
cc2	6.49
cc3	4.29
cc4	3.87
cc5	3.64
cc6	2.17

Table 4.1: Values of the stray capacitance for the C_{ac} measurement.

This is an equation with two unknown variables. Therefore, the oxide thicknesses cannot be calculated exactly. The only way is to assume a value for the thickness of the Si_3N_4 layer and calculate the thickness of the SiO_2 layer (or vice versa). This can be done for STM sensors by

$$d_1 = \varepsilon_0 \varepsilon_{SiO_2} \left(\frac{A}{C_{tot}} - \frac{d_2}{\varepsilon_0 \varepsilon_{Si_3N_4}} \right) \quad (4.4)$$

using $\varepsilon_{SiO_2} = 3.9$, $\varepsilon_{Si_3N_4} = 7.5$, $C_{tot} = 17.41$ pF (see section 4.4.1) and $d_2 = 700 \text{ \AA}$. This leads to a SiO_2 thickness of 2260 \AA which meets our initial assumption of 2000 \AA very well. C_{tot} is approx. 30 % higher for HPK in respect to STM. Thus, we conclude that the total thickness of the HPK insulation layer is thinner.

The switching scheme for this measurement is shown in figure 4.5.

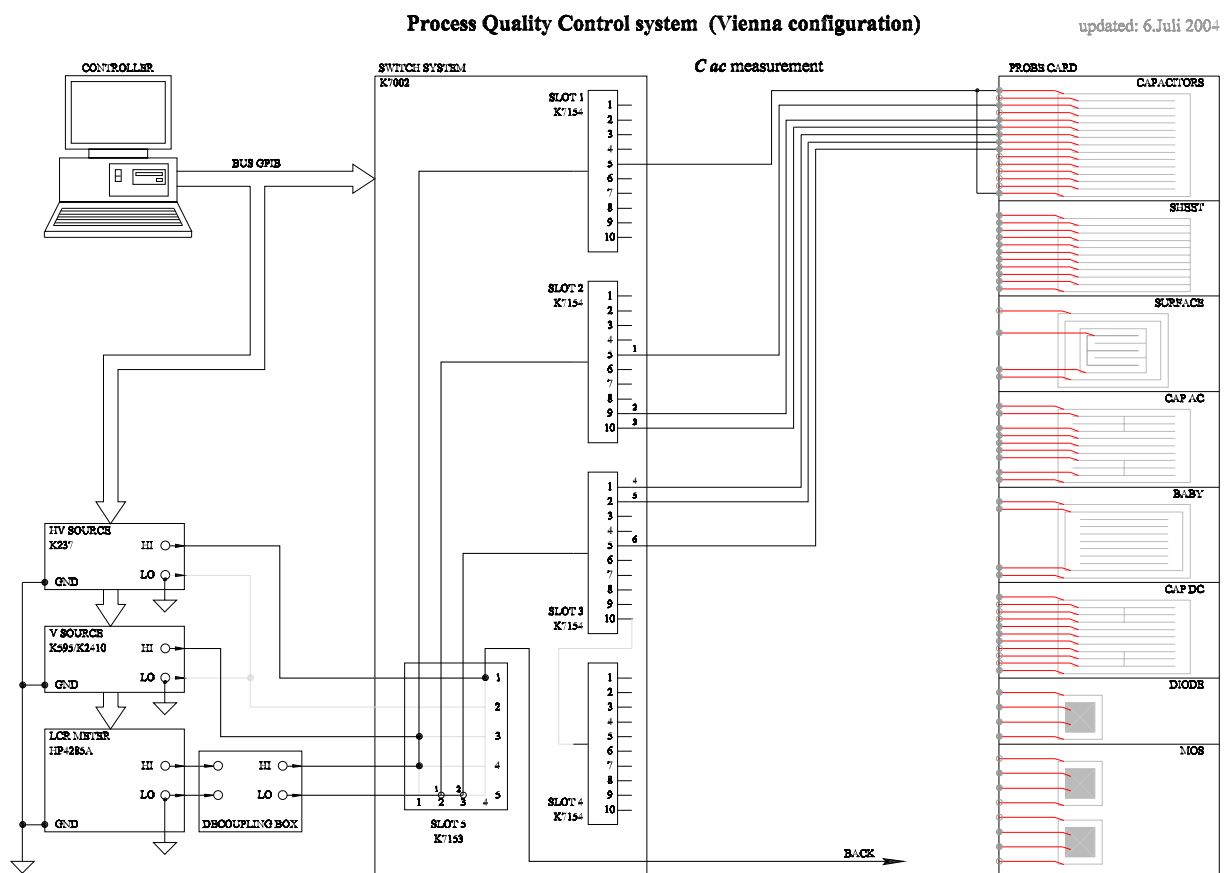


Figure 4.5: Schematics of the Cac measurement.

4.2.2 Dielectric Breakdown (IV_{diel})

The other parameter we can study in the *TS-CAP* structure is the breakdown voltage of the dielectric, corresponding to the maximum voltage that can be applied across the dielectric before a substantial current flows from the p^+ implant to the metal pad.

Contrary to the breakdown of the silicon bulk, which is caused by avalanche effects of the charge carriers, the effect of the breakdown of the dielectric is caused by stripping electrons from their atoms. Every impurity of the oxide can serve as the nucleation point for this breakdown effect.

The measurement is performed by applying GND to the bias ring and a negative HV to the metal pads (up to -200 V in -10 V steps). When the current limit (and thus the dielectric breakdown) is reached, the measurement is stopped for that strip. The breakdown causes irreversible damage to the crystal structure and therefore this destructive test cannot be done on the real sensor.

The upper limit specified for the dielectric current is 10 nA at 120 V. Furthermore, the dielectric must not break below this voltage. The switching scheme is shown in figure 4.6.

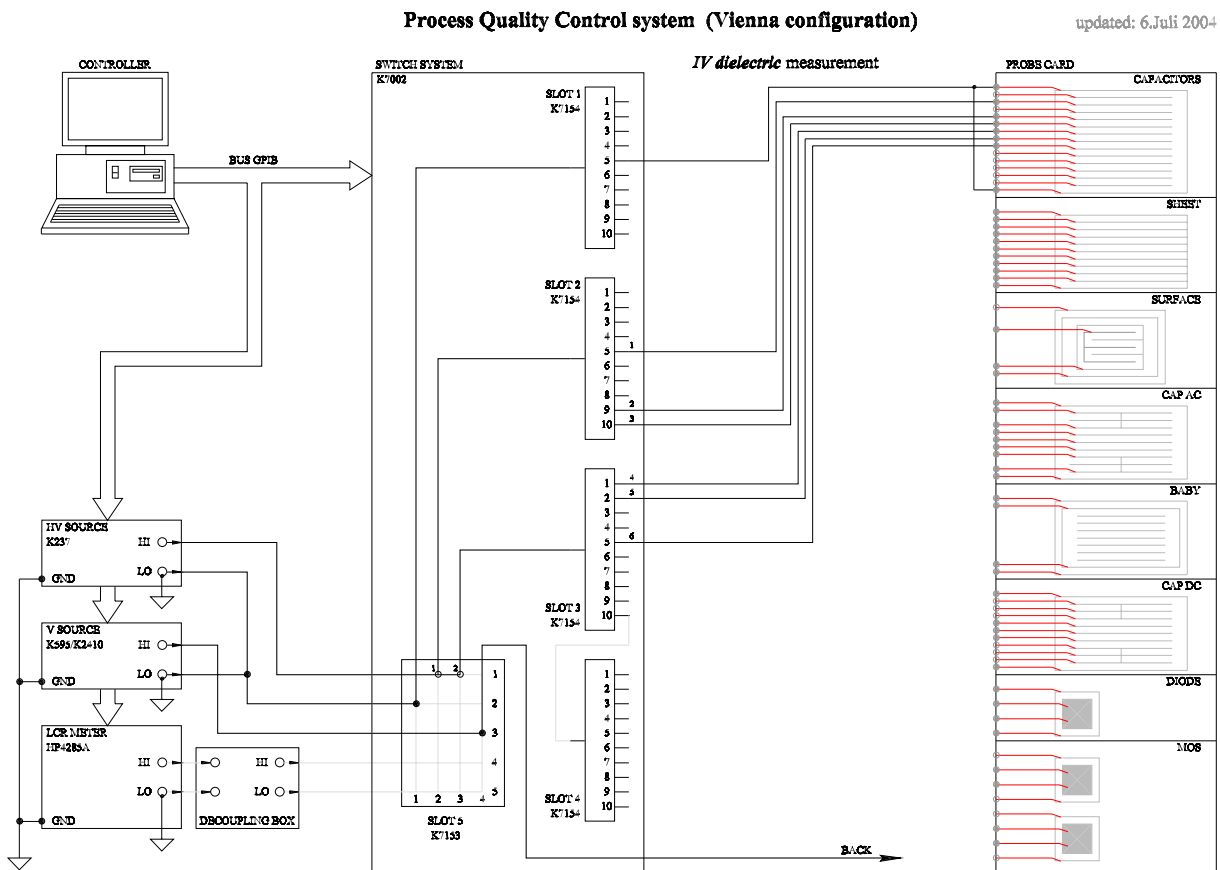


Figure 4.6: Schematics of the IVdiel measurement.

4.2.3 Flatband Voltage (CV_{MOS})

One *metal oxide semiconductor* (MOS) structure (MOS1) is used to measure the flatband voltage V_{fb} through a CV plot. This MOS structure consists of the same SiO_2 oxide layer as the thick interstrip layer. This measurement shows how the interface mobility charge underneath the gate reacts to an applied bias voltage. Figure 4.7 shows the layout of this structure.

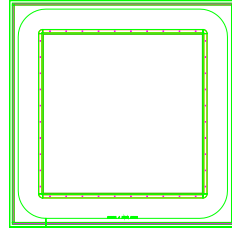


Figure 4.7: Layout of *MOS* structure.

We apply the bias voltage to the backplane while keeping the gate to ground. Therefore, our sign convention is different from what we normally find in literature. Starting from a negative bias voltage of -10 V, we can identify three regions (see fig. 4.8 and fig. 4.9):

accumulation ($V_{gate} > V_{fb}$): free electrons are accumulated beneath the gate. The measured capacitance is the oxide capacitance C_{ox} only. Therefore, the oxide thickness can easily be extracted from this value.

depletion ($V_{gate} \leq V_{fb}$): rising the voltage, the Si region underneath the gate depletes of free electrons. The capacitance decreases until the complete absence of charges in the silicon bulk. In a theoretical situation (as shown in the figures), this happens close to zero: $V_{fb} \approx 0$ V. The shift of the flatband voltage measures the trapped positive charge in the oxide. This is the main parameter we are interested in.

inversion ($V_{gate} << V_{fb}$): holes accumulate beneath the metal gate.

From the CV curve, two parameters are extracted by linear fits: V_{fb} and C_{ox} . With the V_{fb} value, we can calculate the oxide charge:

$$V_{fb} = \phi_m - \phi_s - \frac{Q_{ox}}{C_{ox}} \quad (4.5)$$

where ϕ_m and ϕ_s are the work functions of metal and semiconductor, respectively. For an aluminium gate layer and n-type silicon with a doping in the range of $10^{11} - 10^{12} \text{ cm}^{-3}$ the work function difference $\phi_{ms} = \phi_m - \phi_s$ is around -0.5 V. The oxide charge concentration can be calculated using

$$Q_{ox} = q N_{ox} A_{gate} \quad (4.6)$$

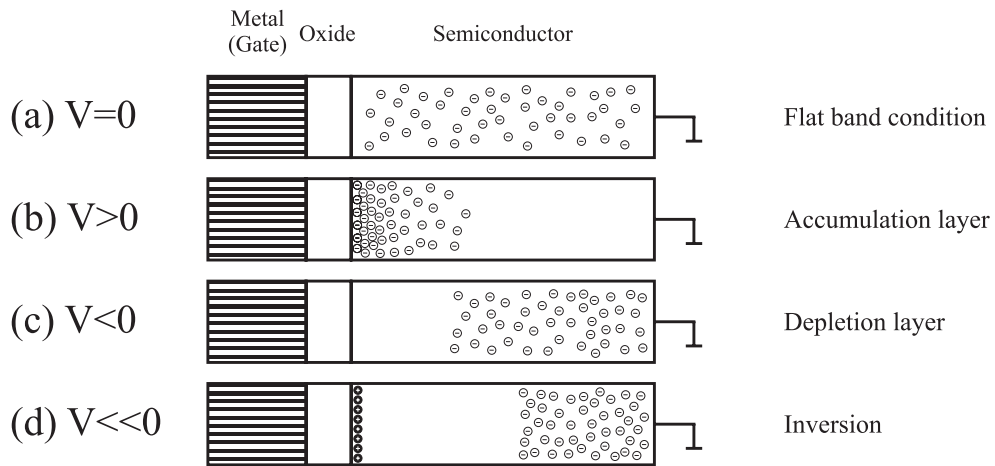


Figure 4.8: States of an "ideal" ($V_{fb} = 0$) n -type MOS structure: thermal equilibrium (a); accumulation (b); depletion (c); inversion (d)

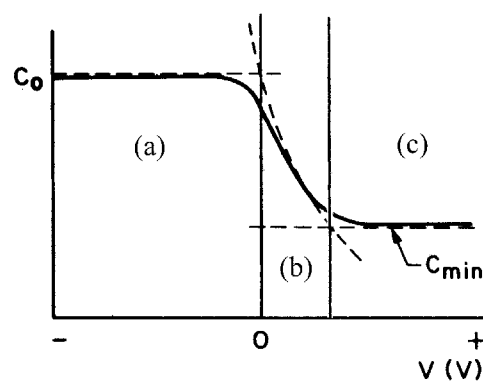


Figure 4.9: CV curve for a MOS structure at high frequency: accumulation (a); depletion (b); inversion (c). For low frequencies, the capacitance rises in the inversion region again up to C_0 .

which leads to

$$N_{ox} = \frac{C_{ox}}{q A_{gate}} (\phi_{ms} - V_{fb}) \quad (4.7)$$

Taking the different sign notation into account, this equation becomes

$$N_{ox} = \frac{C_{ox}}{q A_{gate}} (-0.5 \text{ V} + V_{fb_measured}) \quad (4.8)$$

The second MOS device on the standard teststructure (MOS2), is different between HPK and STM manufactures. In HPK it is just a replica of the first one. In STM it represents the composition of the dielectric of strips (called *MOS-2000*). The gate is built of two SiO_2 and Ni_3O_4 layers, separated by a thin polysilicon layer and covered by a metal contact. For this dielectric configuration, the work function difference ϕ_{ms} has to be calculated using equation 4.9 instead of using the value for the first MOS structure.

$$\phi_{ms} = 0.56 \text{ V} + \frac{k_B T}{q} \ln \left(\frac{N_D}{n_i} \right) \quad (4.9)$$

With the polysilicon concentration N_D in the order of 10^{20} cm^{-3} , ϕ_{ms} is about 0.6 V at room temperature.

The schematics of this measurement is printed in figure 4.10.

Since the MOS-2000 structure is not implemented in HPK teststructures, its measurement is not included in the standard PQC test.

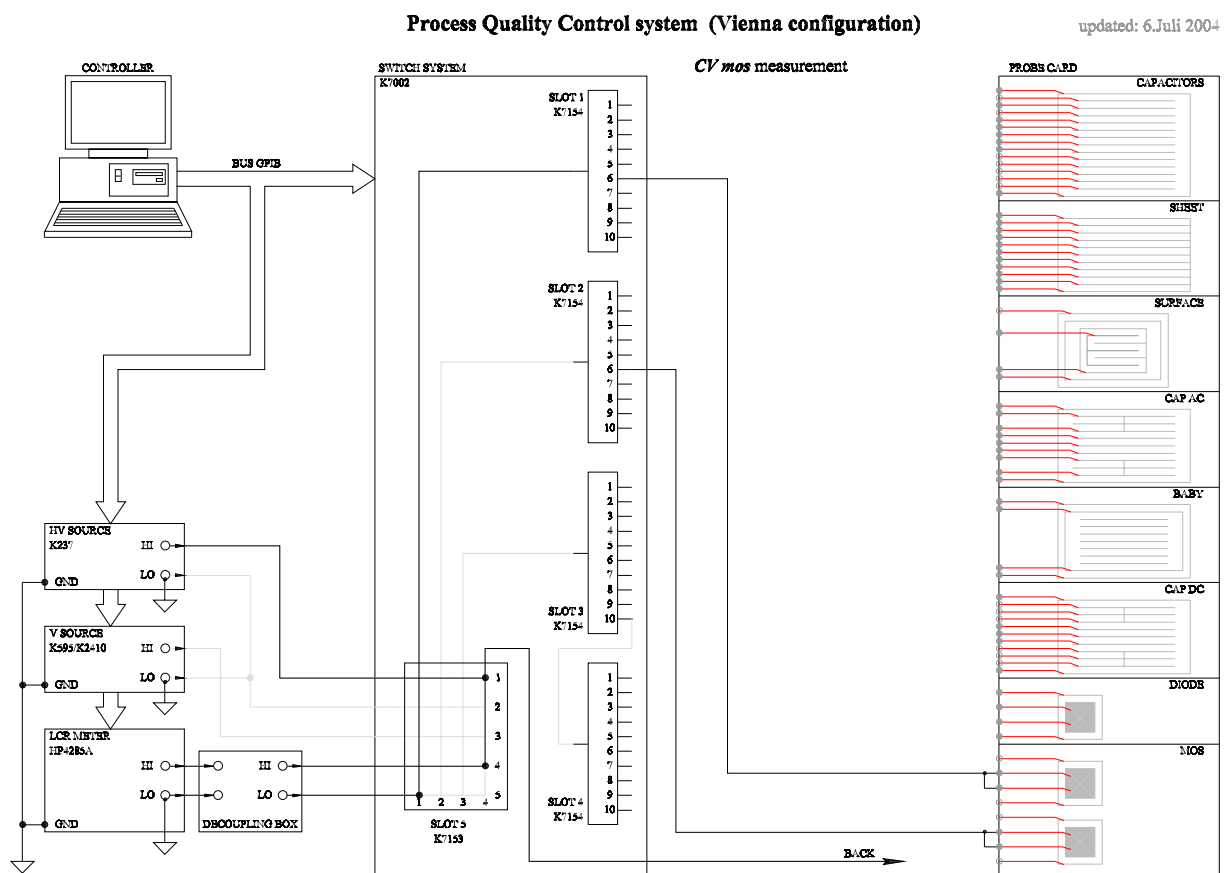


Figure 4.10: Schematics of the CVmos measurement.

4.2.4 Surface Current I_{surf} and Gate Controlled Diode (IV_{GCD})

The surface current is measured to determine the interface recombination velocity and the interface state density [36]. This measurement is done on a structure hosting 4 *gate controlled diodes* (GCD's), two circular and two square ones (see figure 4.11). Our stan-

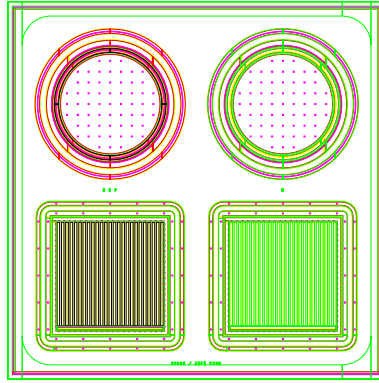


Figure 4.11: Layout of *GCD* structure. In our setup, the right square is used.

ard measurement is carried out on the right square GCD which is built of comb-shaped p^+ implanted strips intertwined with comb-shaped strips made of MOS material. This is in contrast to the left square GCD, where the p^+ strips are replaced by polysilicon ones. The SiO_2 layer in the MOS region corresponds to the oxide in the interstrip region of the real sensor with a thickness of 14000 Å (for STM).

A constant reverse bias voltage V_{bias} is applied to the diode between the backplane and the p^+ strips, while the current through this diode is measured as a function of the gate voltage V_{gate} . In our case, the backplane is grounded, the bias voltage is -5 V and the gate voltage varies between +5 and -20 V with respect to the the backplane potential. The switching scheme is shown in figure 4.12.

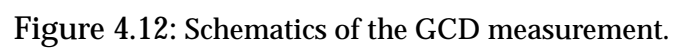
The measured current through the diode is a superposition of two components:

$$I_{\text{measured}} = I_{\text{surf}} + I_{\text{jd}} \quad (4.10)$$

While the bulk current remains constant during the measurement, the surface current varies, caused by a depletion zone which is developed underneath the gate. The effect is similar to the flatband voltage issue (see previous section 4.2.3) and consists of three regions:

accumulation: If V_{gate} is less than V_{fb} , only the volume generation current I_{jd} arising from the pn -junction is observed. The electrons which are induced by the static oxide charge beneath the gate are preventing the reverse voltage to completely deplete the volume.

depletion: When V_{gate} reaches V_{fb} , a depletion region under the gate strips is formed which connects to the depletion region of the diode. This effect is caused by the repulsion of the free electrons underneath the gate by the negative gate potential. Now the generation-recombination-centers at the $\text{Si} - \text{SiO}_2$ interface contribute to the total current, visible as a sharp increase.



inversion: If $V_{\text{gate}} > V_{fb} + V_{\text{bias}}$, an inversion layer under the oxide consisting of electrons is formed, which crushes out the depletion region. This is seen in a sharp decrease of the total current. Higher negative gate voltages do not change this state anymore.

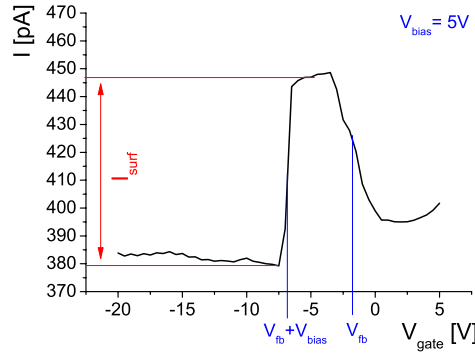


Figure 4.13: Diagram of the surface current measurement. The region are accumulation (right), depletion (middle), inversion (left).

The analysis software extracts the surface current from the measured curve (see fig. 4.13) as the difference of the current level at inversion to the current during depletion and calculates the interface recombination velocity S_0 using

$$S_0 = \frac{I_{\text{surf}}}{n_i e A_{\text{gate}}} \quad (4.11)$$

where e is the elementary charge, $n_i = 1.45 \cdot 10^{10} \text{ cm}^{-3}$ the intrinsic carrier density and $A_{\text{gate}} = 2.3 \cdot 10^{-2} \text{ cm}^2$.

A high value of the surface current indicates oxide contamination problems during the manufacturing of the sensors and thus can induce problems during operation when further charges are introduced by irradiation into the oxide layer.

By the help of irradiation tests the limits for both, the surface current and the flatband voltage were determined. To ensure a stable sensor behaviour in respect to oxide breakdown, the surface current limit was set to 100 pA and the flatband voltage to 10 V. Because we never observed V_{fb} values above 1.5 V for HPK the limit was further reduced to 3 V for this vendor.

4.2.5 Sheet Resistances

Measurements at a structure called *sheet* (see fig. 4.14) are foreseen to determine some important resistance values. It consists of nine sheet structures used to measure the resistivity of the aluminium layer, of the p^+ implant and of the polysilicon resistors. All nine structures have individual contacts at the bottom of the device, whereas the other side is connected to the common bias ring.

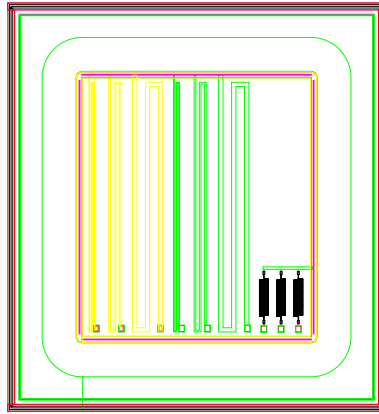


Figure 4.14: Layout of *sheet* structure: aluminium, p^+ implant, polysilicon resistors (from left to right).

Aluminium Resistivity

The resistivity of the aluminium is estimated with the first set of three strips, containing 50, 20 and 10 μm wide strips of the same length. The measured resistance scales with the length and the inverse of the width. The specific resistivity $\rho/sq.$ in $[\Omega/sq.]$ can be calculated using equation 4.12, knowing the ratio of width to length w/l and the contact resistance of the measurement setup R_0 .

$$\rho/sq. = (R - R_0) \cdot \frac{w}{l} \quad (4.12)$$

The subtraction of the contact resistance R_0 is very important for this measurement, since the expected values vary in the range of 5 - 30 Ω for the three strips. Every additional resistive contribution of probecard, contacts or cables affects the result considerably. A correction is made by shorting the needles of the probecard on the large metal layer of the MOS structure. The obtained value is around 4 Ω . Nevertheless, the measurement result depends of the contact quality between the needles and the metal pad. In order to achieve a good contact it is essential to push the probecard up to 20 μm closer to the structure surface than the point of the first contact. The CMS specification for this parameter is $< 25 m\Omega/sq.$ The PQC limit was set to 30 $m\Omega/sq.$ to take instrumental uncertainty into account.

The strip resistance is extracted by a linear fit from an IV-curve with a voltage from 5 to 25 mV in steps of 5 mV. The fit helps to avoid mistakes caused by possible offsets in the voltage.

Implant (p^+) Resistivity

The same procedure as described for aluminium is used to determine the specific resistivity of the p^+ implant. For this purpose, the second set of three strips is used. Since the resistance values are in the range of $200 \text{ k}\Omega$, the influence of the contact resistances can be neglected for this particular measurement.

The limit for this parameter is $400 \text{ }\Omega/\text{sq.}$

Polysilicon Resistance

While the result of the previous sheet measurements are specific resistivities, the result of the polysilicon measurement is a particular resistance value. This is caused by the fact that the size of the polysilicon resistors used in this structure has the same size as the resistor used for the biasing of the sensor itself. Therefore, all three resistors in this structure have the same nominal value. We measure their resistances by applying 1 V between the bias ring and their contacts. The measured values must meet our specification of $1 - 2 \text{ M}\Omega$. Figure 4.15 shows the schematics for this measurement.

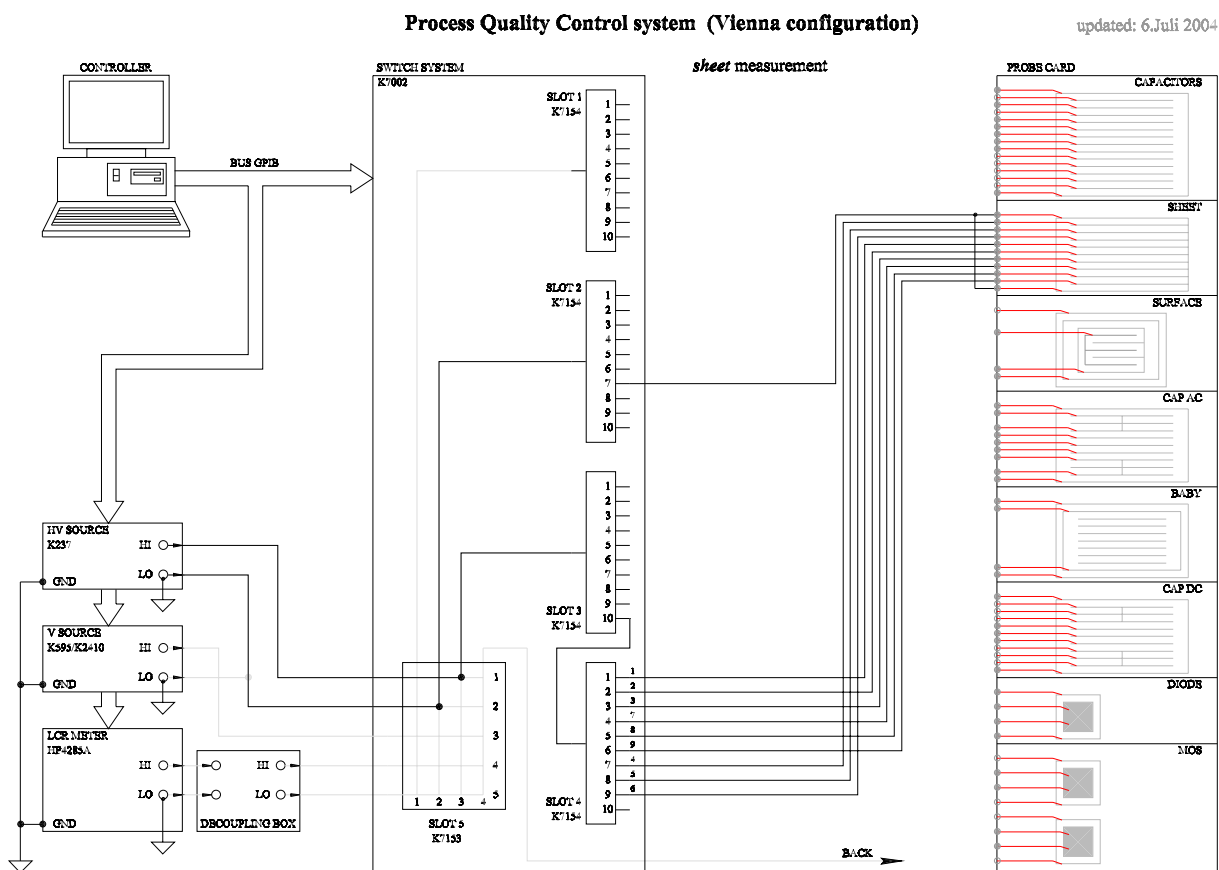


Figure 4.15: Schematics of the sheet resistances measurement.

4.2.6 Interstrip Capacitance (C_{int})

The interstrip capacitance is an important parameter related to the readout electronics. A higher value leads to higher detector noise and thus lower SNR.

The measurement of the interstrip capacitance is done by connecting the *HI* connector of the LCR meter to a central strip, while the *LO* terminal is connected to the two neighbouring strips of the *CAP-TS-AC* structure. The outermost set of three strips on either side of the structure is connected to ground. The layout of the structure is shown in figure 4.16. It is operated now at a reverse bias voltage of $V_{bias} = 400$ V. During com-

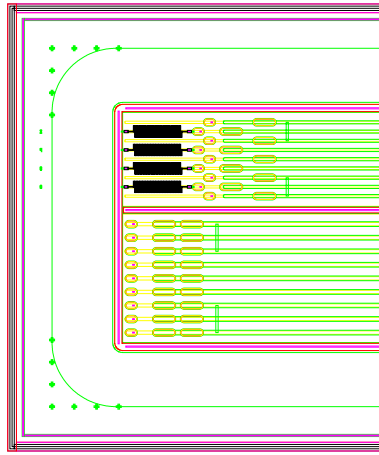


Figure 4.16: Layout of C_{int} structure.

missioning we used a bias voltage of 20 V, which is lower than the depletion voltage, but was expected to be enough to deplete the superficial layers and to measure the interstrip capacitance. Studies have shown that this is not true for STM sensors.

The parametrization in equation 4.13 is the result of a study which investigated the value of C_{int} in respect to different strip geometries [25].

$$C_{int}(\text{per strip}) = a + b \cdot \frac{w + 23 \mu\text{m}}{p} \quad [\text{pF/cm}] \quad (4.13)$$

The strip width w , the pitch p and the parameters a and b are given in table 4.2.6 for the *CAP-TS-AC* structure of thin and thick sensors, respectively. Using equation 4.13

width (p^+ implant) w	=	$30 \mu\text{m}$
pitch p	=	$122 \mu\text{m}$
a_{thin}	=	0.1
a_{thick}	=	0.3
b_{thin}	=	1.6
b_{thick}	=	1.4

Table 4.2: Parameters used to determine the nominal C_{int} values.

and the strip length of the structure (10.17 mm), we find values of $C_{int} = 0.809$ pF

The diagram illustrates the Vienna configuration of the Process Quality Control system. It features a central 'SWITCH SYSTEM K7002' with five slots (SLOT 1 to SLOT 5). Each slot is connected to a 'PROBE CARD' which contains various components: CAPACITORS, SENSORS, SURFACE, CAPAC, BABY, CAPDC, DIODES, and MOS. The system is controlled by a 'CONTROLLER' connected via 'BUS GPIB'. A 'C int measurement' block is also shown. The diagram includes a 'DB COUPLING BOX' and a 'LOW NOISE AMPLIFIER' connected to the switch system and the probe card. A 'BACK' arrow points from the probe card back to the switch system.

Figure 4.17: Schematics of the Cint measurement.

4.2.7 Depletion Voltage and Resistivity (CV_{diode})

Using a simple diode, we are able to determine the wafer thickness or the silicon resistivity through a CV curve. The silicon bulk is biased by a voltage varied between 0 and 300 V, where the capacitance is measured at steps of 5 V. Two linear fits are applied to the $1/C^2$ curve as a function of the applied voltage. The shape of this curve is linear until full depletion is reached. Then the capacitance reaches a plateau and the curve becomes a horizontal line. The depletion voltage corresponds to the intersection of the two linear regions (see figure 4.18).

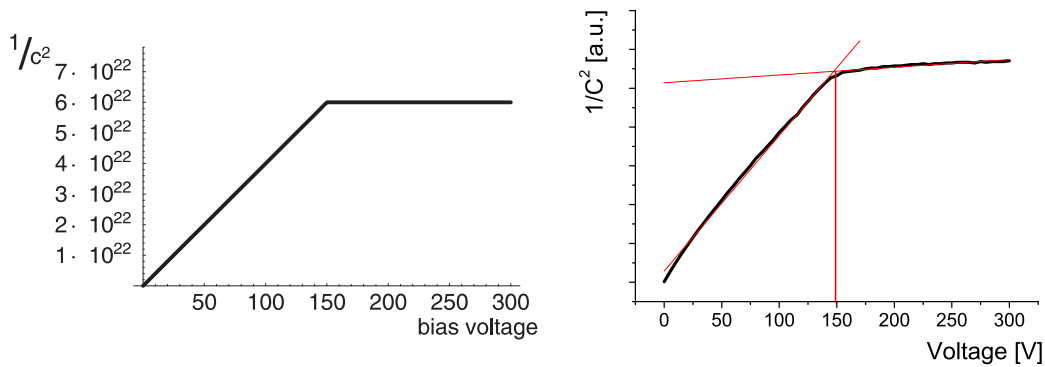


Figure 4.18: Calculated (left) and measured (right) CV curves with linear fits (red) to determine the depletion voltage. The plots show the function $1/C^2(V)$ with a depletion voltage of 150 V.

The area of the diode surface is needed to calculate the interesting parameters (see figure 4.19 and table 4.3). It is better defined when the guard ring is tied to ground. Taking into account that the field lines extend into the intermediate region between the implanted square and the guard ring, half of the intermediate area is added to the implant for the following calculations.

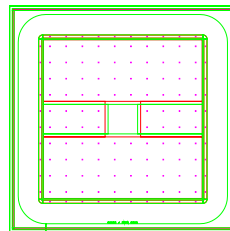


Figure 4.19: Layout of the diode structure.

Because of geometrical reasons, the depletion voltage measured with this structures differs to a sensor with the same size but segmented strips [37]. Thus, comparing the depletion voltages of the sensor and the teststructure, one has to take this geometric factor into account (approx. $V_{\text{depl (Sensor)}} \approx 1.2 \cdot V_{\text{depl (Diode)}}$).

side length of inner square:	4920 μm
distance between inner square and guard ring:	40 μm
guard ring width:	100 μm
side length used for calculation of active area:	4960 μm

Table 4.3: Dimensions of the diode structure.

The depletion depth is calculated by using an equation derived from the well know parallel plate capacitor (equation 4.2). C_{depl} is calculated by subtracting the stray capacitance of the setup from the measured capacitance value at full depletion. In our setup, the typical stray capacitance of the setup is 2 pF, which reduces the measured 8 pF (for thick STM sensors) to 6 pF.

The bulk resistivity is calculated as

$$\rho = \frac{d_{\text{nominal}}^2}{2 \varepsilon_0 \varepsilon_r \mu_e V_{\text{depl}}} . \quad (4.14)$$

The limits of the capacitance and the depletion voltages can be derived from the specified resistivity and nominal thickness requested for the sensors. The calculated values are shown in table 4.4.

HPK:	nominal thickness: 320 μm (<i>thin</i>)
	300 < d < 340 μm (thickness variation $\pm 20 \mu m$)
	7.5 pF < C_{depl} < 8.6 pF
	5 pF < C_{depl} < 10 pF (measurement limits used for PQC)
	1.5 < ρ < 3.0 k Ω /cm
	119 V < V_{depl} < 238 V
	100 V < V_{depl} < 250 V (measurement limits used for PQC)
STM:	nominal thickness: 500 μm (<i>thick</i>)
	300 < d < 340 μm (thickness variation $\pm 20 \mu m$)
	4.9 pF < C_{depl} < 5.3 pF
	3 pF < C_{depl} < 8 pF (measurement limits used for PQC)
	3.5 < ρ < 7.5 k Ω /cm
	116 V < V_{depl} < 249 V
	100 V < V_{depl} < 260 V (measurement limits used for PQC)

Table 4.4: Nominal specifications of the sensors from the two different suppliers.

The carrier concentration N_{bulk} can be calculated by:

$$N_{\text{bulk}} = \frac{2 \varepsilon_0 \varepsilon_r \mu_e V_{\text{depl}}}{e d} \quad (4.15)$$

During the measurements of the first teststructures we found that this measurement sometimes destroys the coupling capacitors in the C_{ac} structure and sometimes also the GCD. The reason for this behaviour is that the structures which are not measured are floating. This means that the potential at the p^+ implants of these structures can follow the backplane potential (which goes up to 300 V). This causes a potential difference across the dielectric of the coupling capacitors which is much higher than the breakdown voltage. To avoid this problem, we used additional connections between the p^+ and pad contacts shorting the capacitors and thus avoiding a voltage drop across them (*protection*). The contacts 1, 2, 5, 9 and 10 of multiplexer 2 and the contacts 1, 2, 5 and 7 of multiplexer 3 are closed for this protection while figure 4.20 shows the switching scheme for this measurement without protection.

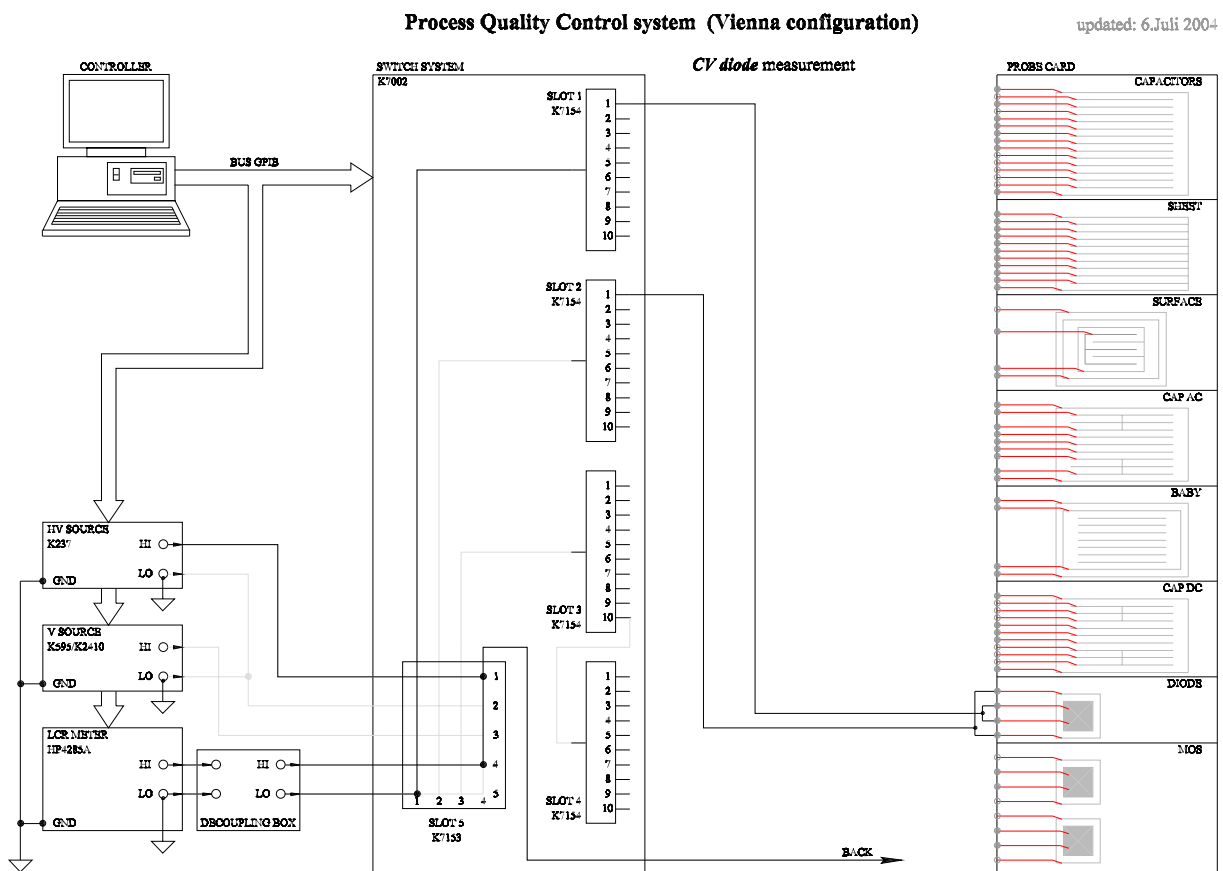


Figure 4.20: Schematics of the CV diode measurement.

4.2.8 Dark Current and Breakthrough (IV_{baby})

A structure with 192 strips at a pitch of $120\ \mu m$ in the center of the teststructure is called baby-sensor (see figure 4.21. The guard ring is not contacted in this setup, as it is not

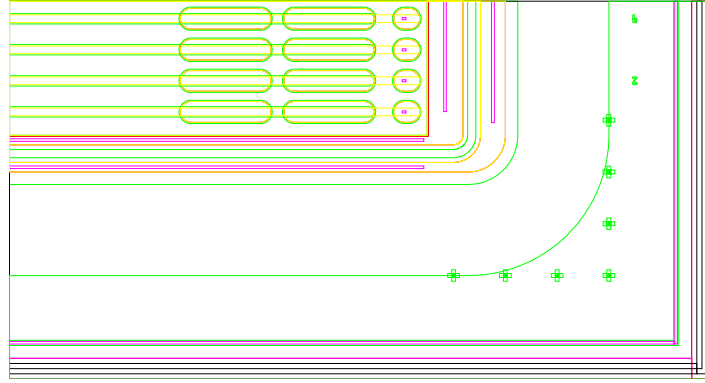


Figure 4.21: One corner of the baby detector structure.

used in the normal operation of the sensors either. The mini-sensor has an active area of $2.3 \times 1.6\ \text{cm}^2$. Our test on this device consists of an IV curve from 0 to 700 V in 5 V steps, from which we extract the breakdown voltage and the current value at 450 V. We compare the results with our limits of $V_{break} > 500\ \text{V}$ and $I(450\ \text{V}) < 1\ \mu\text{A}$.

We encountered similar problems for this measurement as for the CV_{diode} measurement with broken coupling capacitors and broken GCD. Thus, we also used a similar protection by closing the contacts 2, 5, 9 and 10 of multiplexer 2 and contacts 1, 2, 5 and 7 of multiplexer 3. The normal switching scheme without protection is shown in figure 4.22.

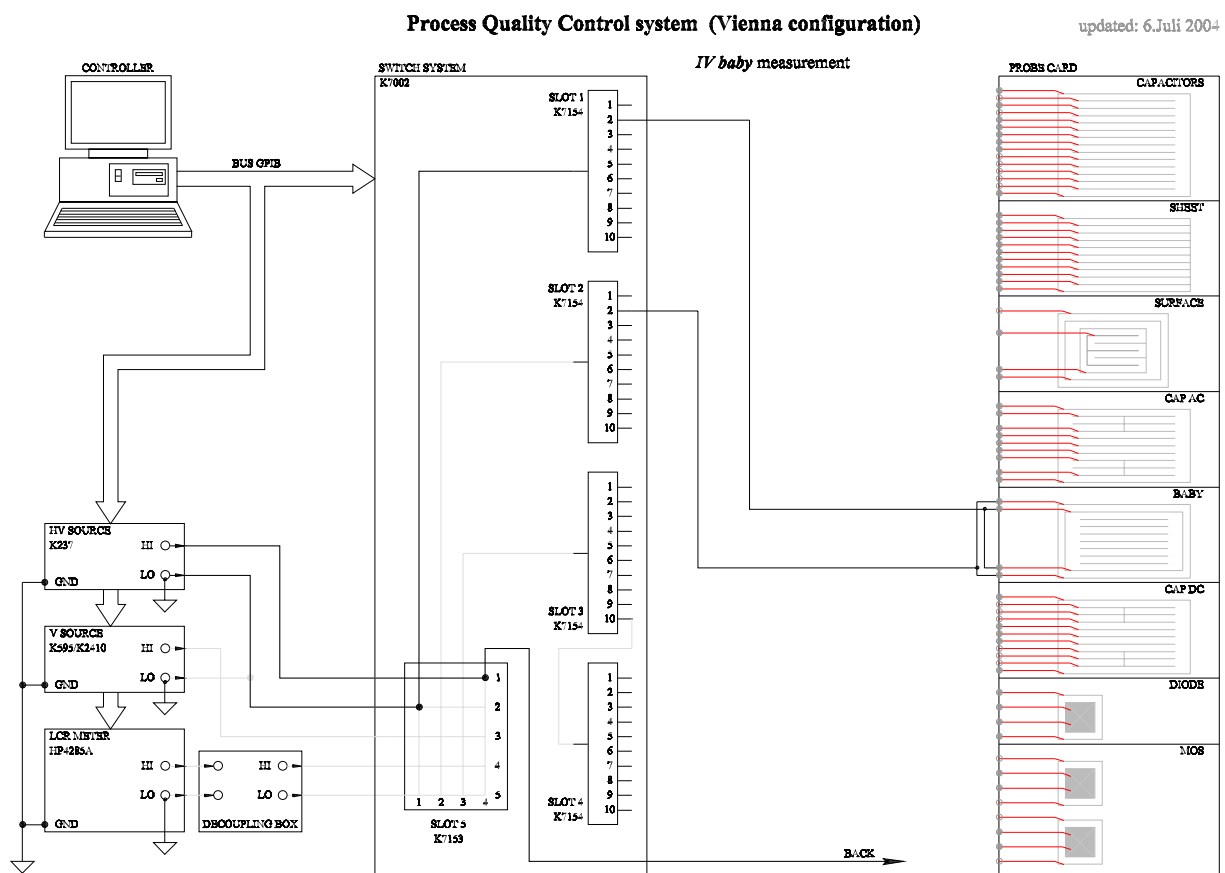


Figure 4.22: Schematics of the IVbaby measurement.

4.2.9 Interstrip Resistance (R_{int})

The *CAP-TS-DC* structure is used to measure the inter-strip resistance. It has the same geometry as *CAP-TS-AC* with two exceptions: the lack of polysilicon resistors avoids their contribution to the measurement, which means that the strips are isolated from the bias ring. Moreover the p^+ implant is directly connected to the metal layer all along the length of the strips through vias (see figure 4.23). Thus the implant layer can be contacted using either DC or AC pads.

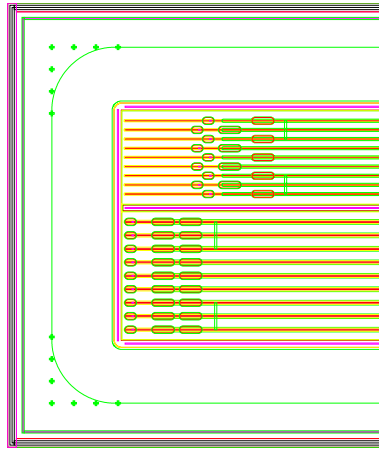


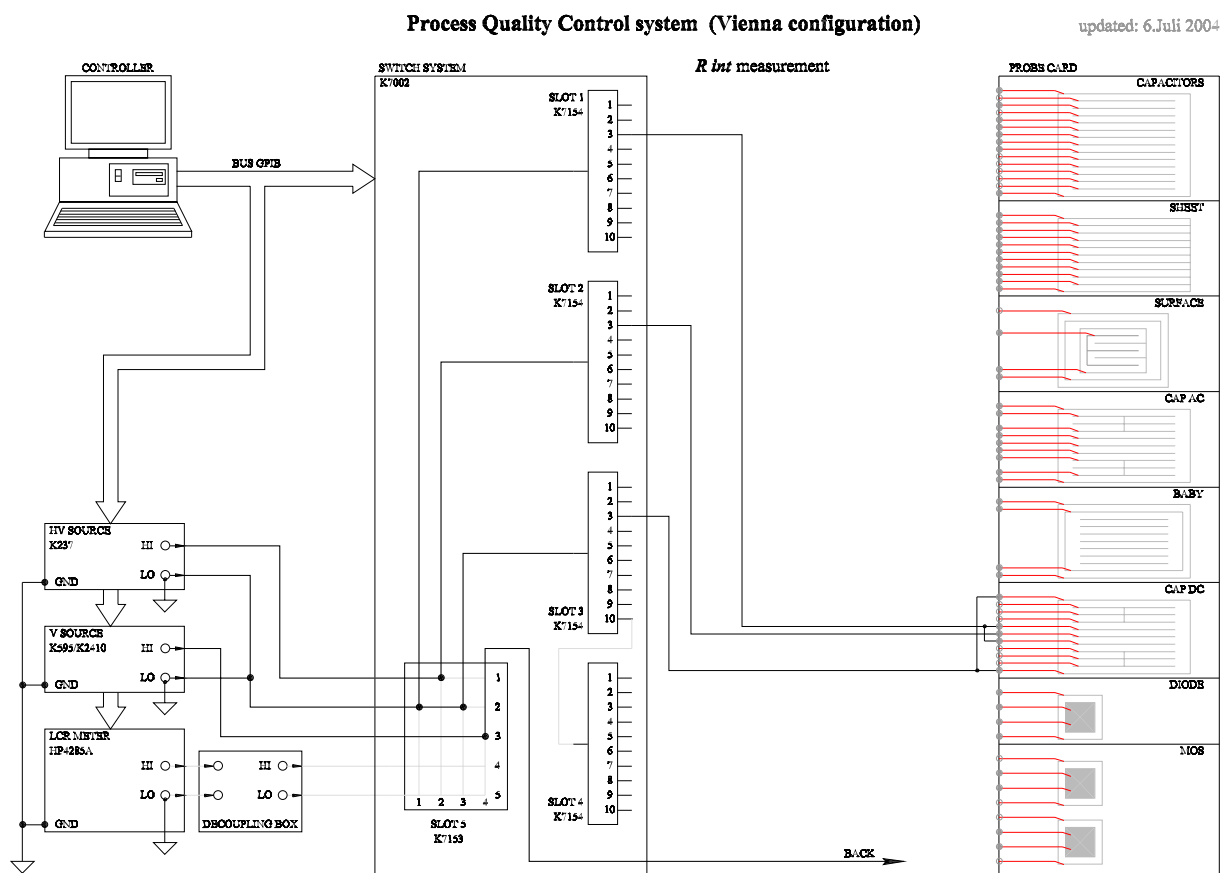
Figure 4.23: Layout of DC coupled strip layout for R_{int} measurement.

The inter-strip resistance is measured between the central strip and its two neighbours (which are tied to ground). The central strip is set to a potential of a few volts and the current between them is measured. The three outermost strips at every side are connected together through their metallization, but it is not foreseen to put them to ground. However, this is done for the bias ring to stop currents flowing from the outside of the structure with malicious influence on the measurement.

The device is inversely polarized with $V_{bias} = 100$ V. This voltage is enough to deplete the interesting region underneath the implants on the p -side. The voltage drop between the central strip and its two neighbours must be kept small in respect to the bias voltage to avoid a perturbation of the depletion field. Since the interstrip resistance should be high, a very low current across the strips of a few pA is expected. Therefore an instrument with a high current sensitivity is needed.

The resistance value is extracted with a linear fit of the IV curve obtained by a voltage scan between ± 2 V. This procedure is more precise than a single measurement because the contribution of a constant leakage current is removed.

Our specification of the inter-strip resistance is $R_{int} > 1$ G Ω .

Figure 4.24: Schematics of the R_{int} measurement.

4.3 Measurement Procedure and Software

A computer running *Labview* [38] is used for data acquisition and measurement analysis. Standalone parts of the Labview application program were written by all involved laboratories. The acquisition part was written in Strasbourg, while Florence is responsible for the input file reader and the fitting procedures. The XML output file generator was developed in Vienna. All parts together build the *common software*. The computer is equipped with an internal PCI card which connects to the instruments via GPIB for control and data retrieval and a serial link to the TRHX system.

A teststructure has to be put onto a mechanical support in the light-tight probestation box. It is held by a vacuum jig. The needles of the probecard are aligned to the contact pads of the teststructure, moving the teststructure on its support using micron positioners while looking through a microscope. After successful alignment, the probecard must be lowered in z direction to establish electrical contact of the needles.

The software is expecting the OBJECT_ID of the teststructure first, which can be entered manually or by the barcode reader. By reading its forth digit, the producer and by the next two digits the geometry of the sensor (IB, OB, W) is determined. With this information, the software reads the correct column of the *input data file* (see table A.2 in the appendix) and sets all measurement parameters and limits. Now the software is ready to start an automatic run, where all of the measurements described in the previous sections are performed in the given order. After each single test, fits are performed and the results are calculated. Finally, all relevant results are shown on the screen, written to *local files* and combined into one single XML file. If everything went well, the XML file can be uploaded into the TrackerDB. If single substructures have to be re-tested, a manual run of dedicated tests has to be started.

A screenshot of the acquisition software showing the main screen after an automatic run has finished is shown in figure 4.25.

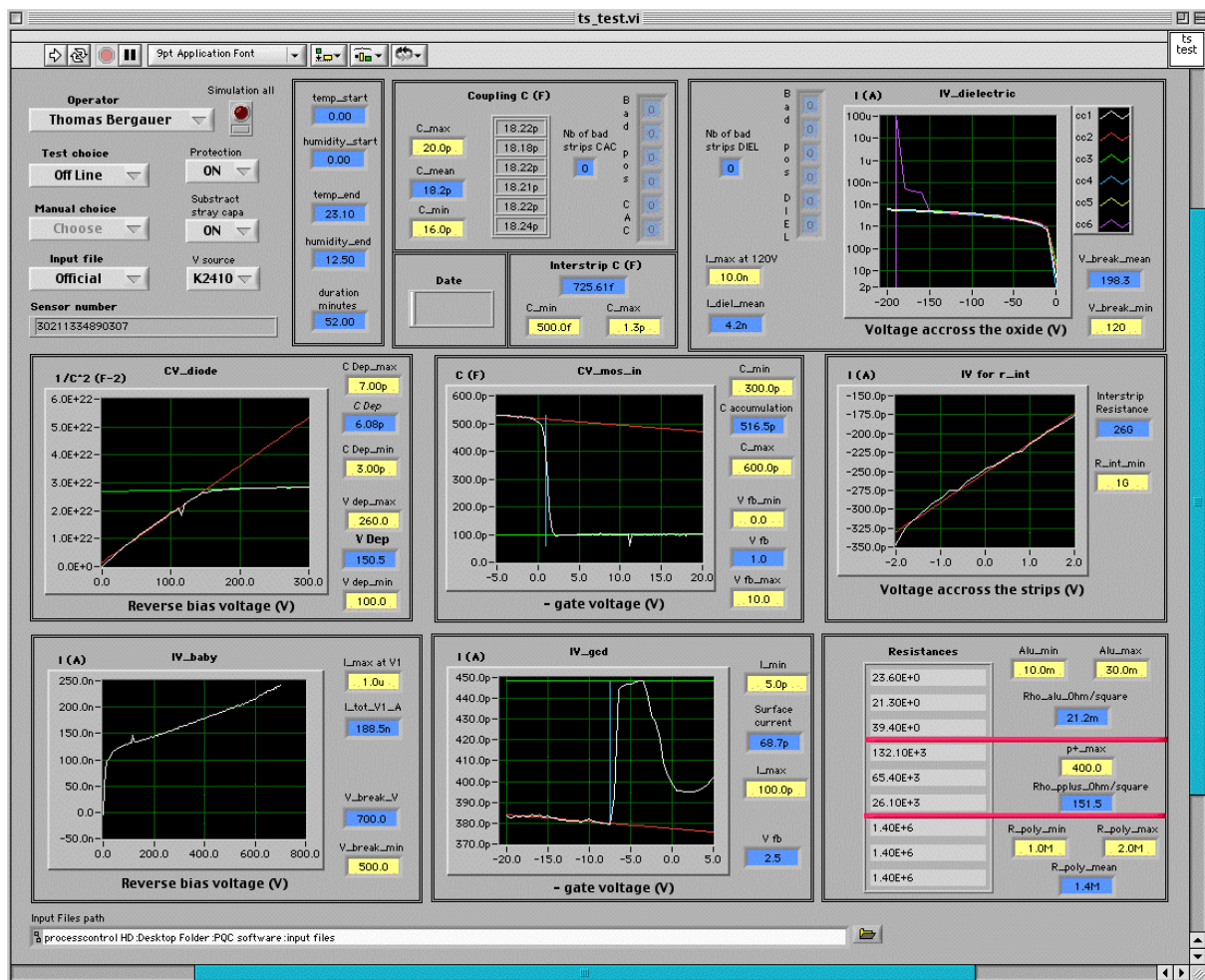


Figure 4.25: Screenshot of the PQC measurement software.

4.4 Measurement Results

Up to now about 900 teststructures have been measured in Vienna. Adding the measurements of the two other labs, data of almost 2700 teststructures exists. The evolution of every measured parameter is shown in diagrams in this section and compared between the two suppliers. The plots have been created querying TrackerDB using self written SQL queries and VisualDB. The tests started in July 2002.

4.4.1 Coupling Capacitance C_{ac}

The coupling capacitance was quite stable during the whole PQC operation for both companies. The different average values of 17.41 pF for STM and 23.01 pF for HPK is because of different oxide thicknesses, which are well within the limits of $16 < C_{ac} < 20$ pF for STM and $18 < C_{ac} < 25$ pF for HPK. The average value of STM matches the assumed oxide layer thickness very well.

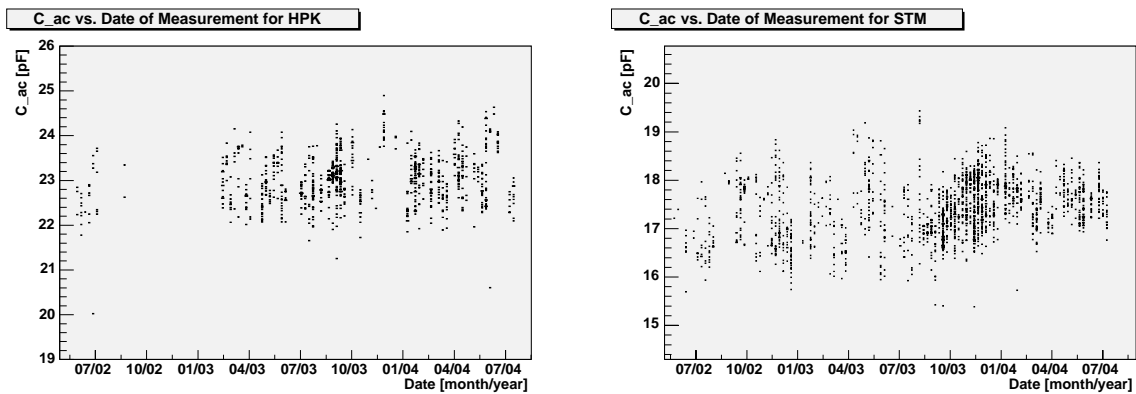


Figure 4.26: C_{ac} for HPK (left) and STM (right) sensors.

4.4.2 Dielectric Current I_{diel}

The dielectric current between p^+ implant and aluminium strip is plotted in figure 4.27 and its breakthrough voltage is shown in figure 4.28. Almost all measurements fulfil the specifications of $I_{diel} < 10$ nA and $V_{break, diel} > 120$ V. We observed humidity dependence of the current for some STM teststructures. Moreover, we observed an average breakthrough voltage of 173 V for HPK, while for STM we often failed to force a breakthrough of the oxide layer up to the ultimate applied voltage of 200 V.

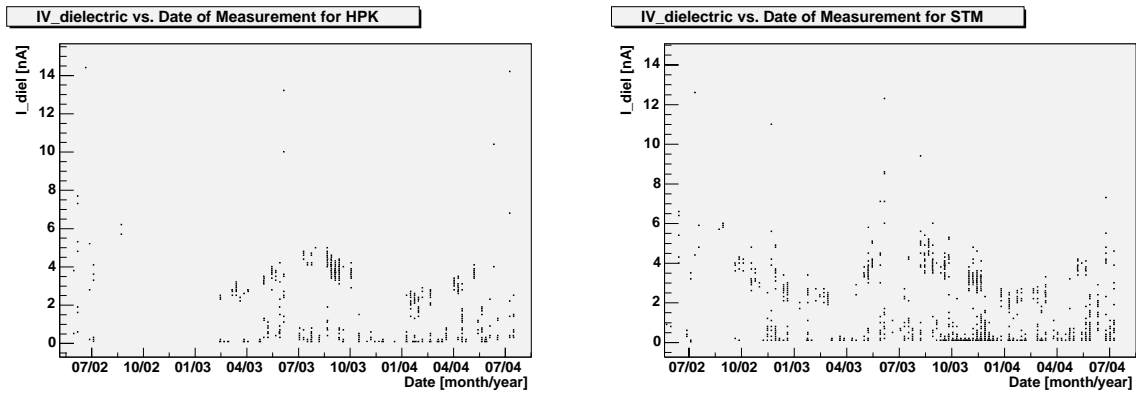


Figure 4.27: I_{diel} for HPK (left) and STM (right) sensors.

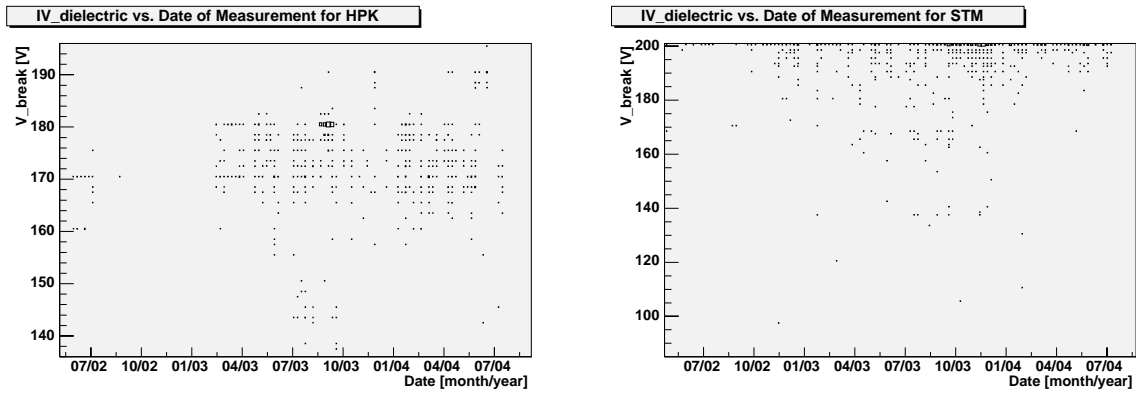


Figure 4.28: $V_{\text{break,diel}}$ for HPK (left) and STM (right) sensors.

4.4.3 Flatband Voltage V_{fb}

While the flatband voltage for HPK has been stable during the whole sensor production at an average of 1.42 V, its value for STM has evolved in time. For their early sensors it was less than 10 V, but increased by the end of 2002 up to 35 V; far above our specified limit, which was relaxed from its initial value of 7 V up to 10 V after an irradiation test has proven no disadvantage in the sensor behaviour. After intervention, STM modified the fabrication process and the value decreased again at around 10 V. In autumn 2003 values up to 20 V have been observed again. Starting with beginning of 2004, this parameter dropped down again and has been stabilised at about 2 V.

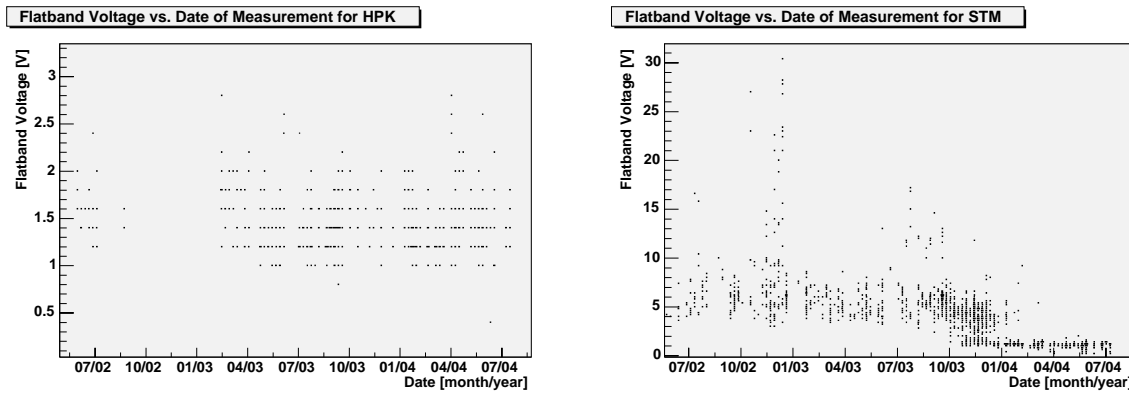


Figure 4.29: V_{fb} for HPK (left) and STM (right) sensors.

4.4.4 Surface Current I_{surf}

The surface current is mostly stable for HPK sensors (between 30 and 80 pA) with rare outliers, while for STM we saw some fluctuations starting in September 2003. Before that, it was stable as well. For later deliveries, a decrease was observed between November 2003 and March 2004 and an increase up to 120 pA afterwards.

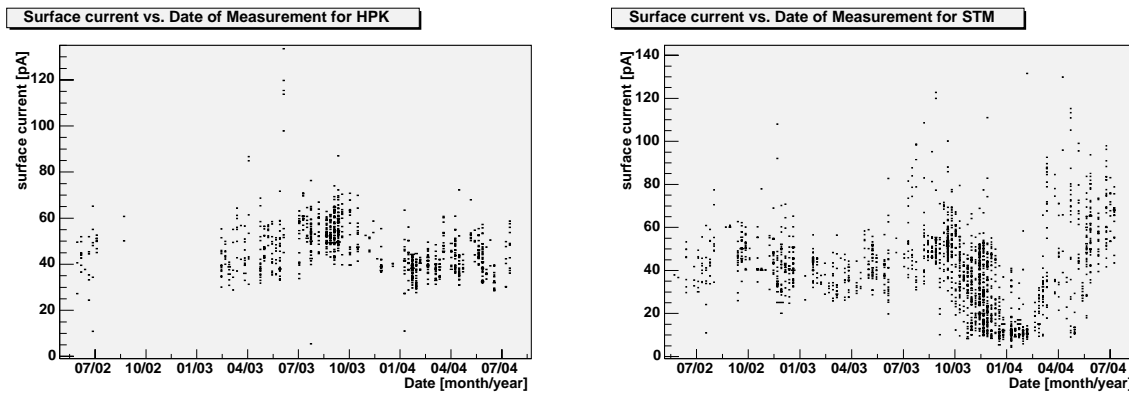


Figure 4.30: I_{surf} for HPK (left) and STM (right) sensors.

4.4.5 Sheet Resistances

Aluminium Resistivity

The values for HPK are between 20 and the upper limit of 30 m Ω /sq. with an average of 23 m Ω /sq. during the total production period, while for STM the values were slightly above the limit until December 2002. After PQC intervention STM increased the aluminium layer thickness from 1.2 to 2 μ m, leading to significantly lower resistivity values with an average of 19.2 m Ω /sq. afterwards.

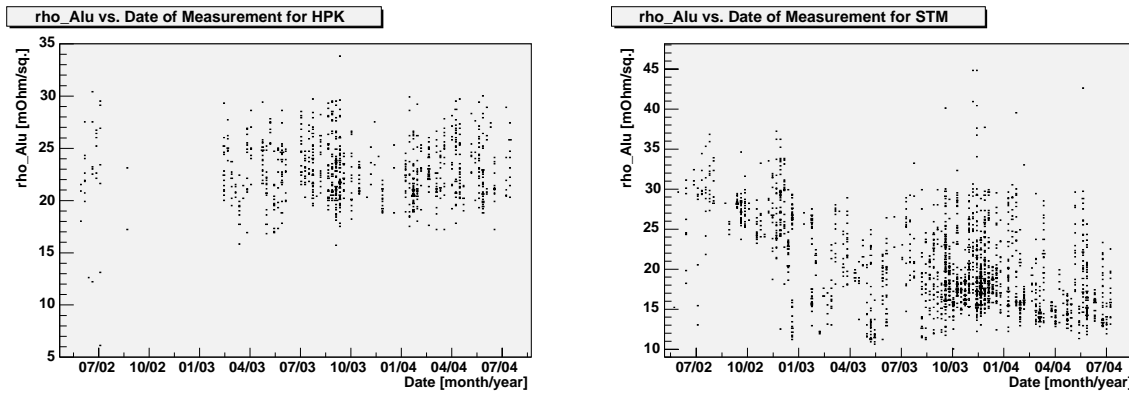


Figure 4.31: ρ_{alu} for HPK (left) and STM (right) sensors.

Implant (p^+) Resistivity

For the p^+ implant resistivity, we found generally stable behaviour within the limit of $\rho_{p^+} < 400 \Omega/\text{sq.}$ In case of STM, its value was quite low in a period between September 2003 and March 2004. This is caused by a very low value of R_{int} , which was also observed during that period (see section 4.4.9) and which influences the p^+ measurement.

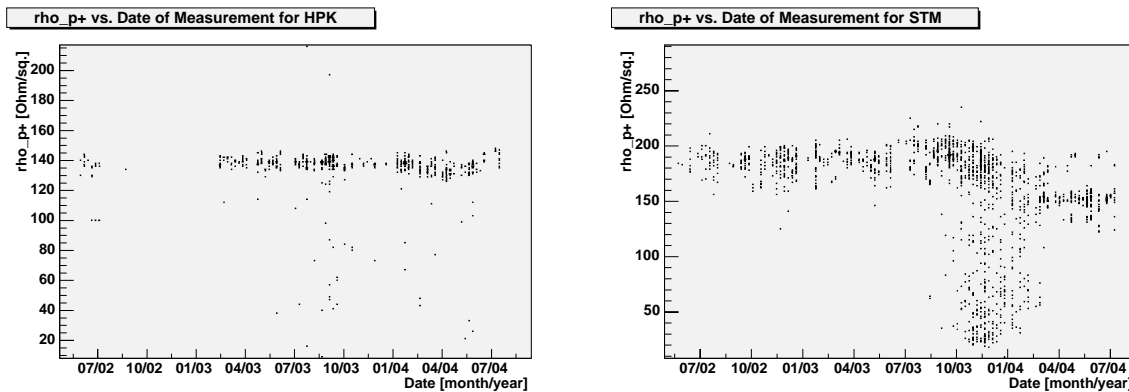


Figure 4.32: ρ_{p^+} for HPK (left) and STM (right) sensors.

Polysilicon Resistance

This parameter was very stable within the limits of $1 < R_{\text{poly}} < 2 \text{ M}\Omega$ for both companies with an average of 1.50 and 1.45 $\text{M}\Omega$ for HPK and STM, respectively. However, an increase to approx. 2.3 $\text{M}\Omega$ has been observed at HPK teststructures between June and July 2004. This change was announced by HPK and accepted by the tracker collaboration.

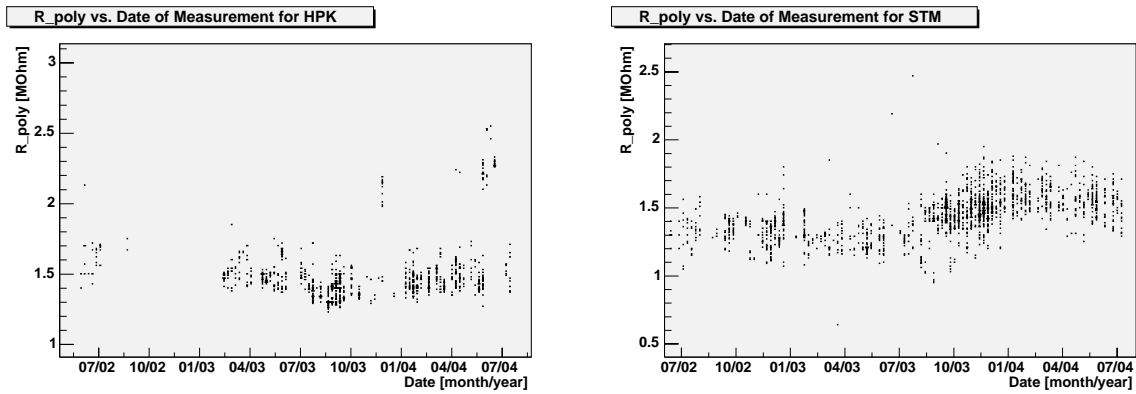


Figure 4.33: R_{poly} for HPK (left) and STM (right) sensors.

4.4.6 Interstrip Capacitance C_{int}

The interstrip capacitance evolution shows a step for both vendors in September 2003. This is caused by increasing the bias voltage which yields more uniform results. After that change, the values for HPK were quite stable, while we still observed some outliers for STM up to the limit of 1.3 pF.

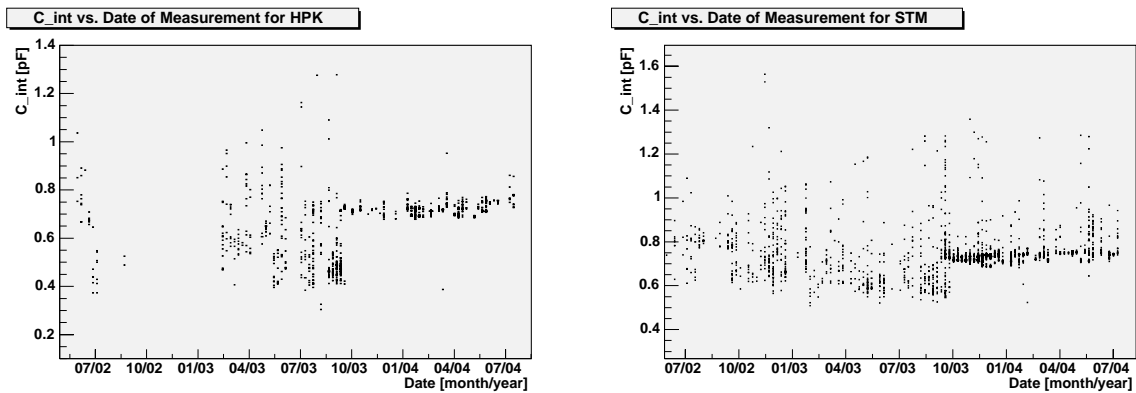
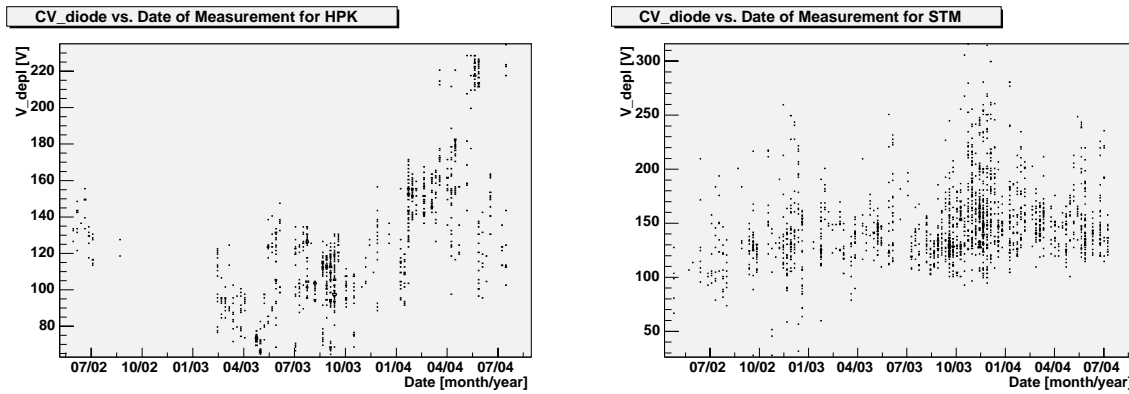


Figure 4.34: C_{int} for HPK (left) and STM (right) sensors.

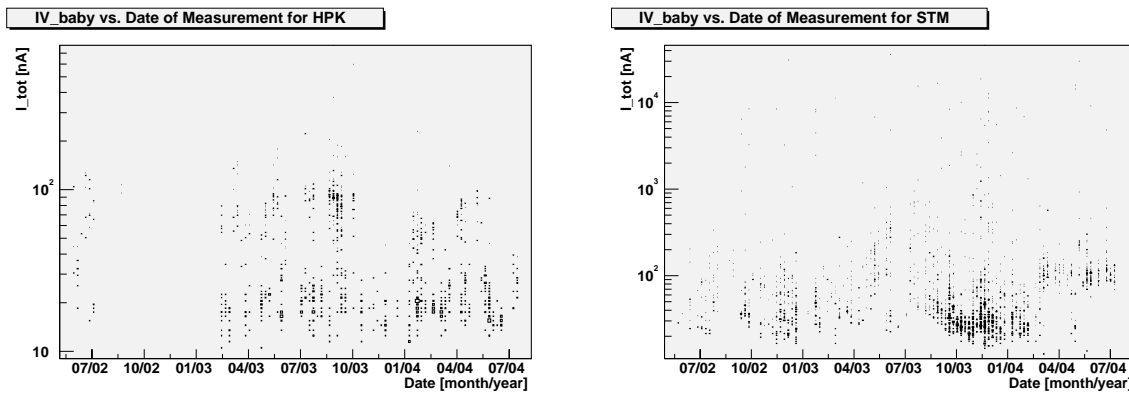
4.4.7 Depletion Voltage V_{depl}

Starting in February 2003, we observed a low depletion voltage for HPK below the specified limit of 100 V. This issue was reported to the company and was addressed after November 2003. Studies have shown that these sensors can still be used in the outer layers of the tracker with lower radiation levels and thus later inversion. We did not observe any abnormal behaviour for STM.

Figure 4.35: V_{depl} for HPK (left) and STM (right) sensors.

4.4.8 Dark Current I_{tot}

The dark current was mostly within the limit of $1 \mu\text{A}$. Outliers were only found for scratched teststructures. Thus, three regions can be seen for STM, one before September 2003, one between September 2003 and March 2004 and one after March 2004. In the middle region, the dark current was significantly lower than in the third region.

Figure 4.36: I_{tot} for HPK (left) and STM (right) sensors.

4.4.9 Interstrip Resistance R_{int}

Finally, the last parameter again reveals a difference between the companies. Since the interstrip resistance is normally in the range of tens to hundreds of $\text{G}\Omega$, it is plotted in logarithmic scale. The spread for HPK shows the different insulation resistors of the setup (cables, probecard, instruments) for the three laboratories. On the other hand, one can see a decrease of the interstrip resistance for STM below the lower limit of $1 \text{ G}\Omega$ in the same period as already obvious in the previous plots. This issue was reported to

STM as a possible passivation problem and was remedied by the company after March 2004.

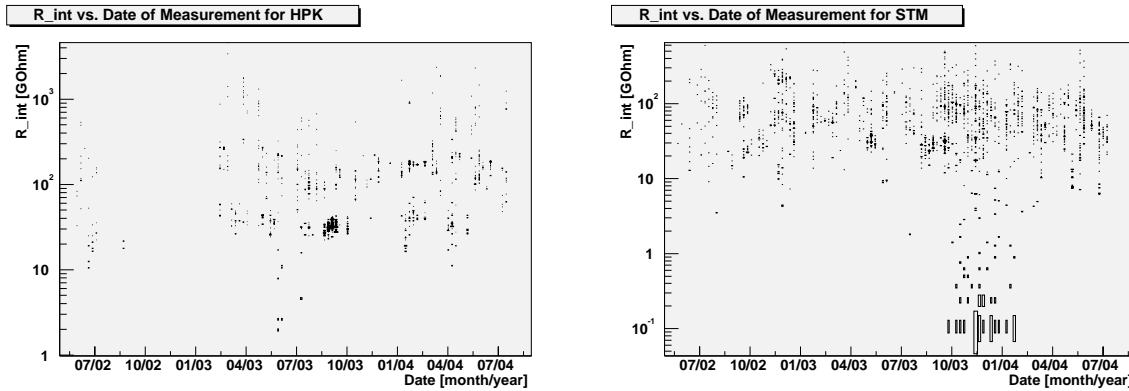


Figure 4.37: R_{int} for HPK (left) and STM (right) sensors.

4.5 Summary of the Results

Summarising these results, the production process of HPK was quite stable over the production period of two years. The issue with low resistivity values was discovered by PQC and corrected by the company after reporting the problem to them. A slightly higher polysilicon resistance was found in agreement with the notification from HPK during the last two months.

For STM, the production process is rather unstable. After troubles with a high flatband voltage in the past, the company changed the oxide layer after intervention from PQC and at the same time introduced problems with a too low interstrip resistance. This issue started in September 2003 and lasted until March 2004 (measurement dates). The corresponding sensors have been delivered between September and November 2003. Mid of April 2004, the Tracker collaboration received batches where STM addressed this issue. Yet, some instabilities remain.

From the experimental point of view the setup was very successful because the other CMS quality assurance procedures were not able to identify most of the issues found at PQC (e.g. high flatband voltage, high aluminium resistivity, low interstrip resistance). Thus the system prevented the use of not fully functional sensors for the CMS Tracker.

Future improvements of the setup and the design of the standard half-moon structures could address some minor disadvantages of the current system: A newly designed sheet structure with a four-wire measurement could suppress contact and other serial resistances and a larger C_{int} structure would lead to higher capacitance results and thus could increase the accuracy of the measurement.

Chapter 5

Long Term Stability Tests

One of the tests of the CMS quality control for the silicon strip sensors is a long term stability test at room temperature [26]. This test is done on a small, but representative sample of all sensors delivered by the two suppliers, HPK and STM. The study of the long term stability of the sensors is necessary because once the detector is installed in the experiment, access will be very limited. Therefore we must ensure that the sensor characteristics and the dark current in particular is very low and stable in time.

Two measurement setups were installed at IReS Strasbourg and HEPHY Vienna to perform standardised long term tests at room temperature. In addition, a third setup has been built in Vienna which offers the same test at a temperature of -10°C . This corresponds to the highest operating temperature allowed for the silicon sensors of CMS [12].

5.1 Measurement Setup

The setup description in this section refers to the Vienna setup, while the electrical configuration of the Strasbourg setup is slightly different.

5.1.1 Setup Description

A light-tight box contains ten plates with a conducting rubber surface, mounted individually on moving slides in a vertical arrangement. The sensors are placed on these plates which are used to provide the backplane contact (see figure 5.1).

The bias ring of each sensor is connected to a pad which provides the connection to the measuring instruments by wire bonding. At top and bottom of the box combined temperature and humidity sensors are located, which are connected to the TRHX system. The humidity is controlled by blowing dry air (5 % relative humidity at room temperature) into the box through an electromagnetic valve, which is driven by the TRHX system in order to keep the relative humidity between 10 and 30%.



Figure 5.1: Photo of the light-tight longterm measurement box containing ten plates mounted on slides supporting the sensors.

A reverse bias voltage of 400 V is applied to each sensor by a source measure unit (Keithley 2410). A resistor of 470 k Ω is connected in series to each silicon sensor. The voltage drop across these resistors is measured by a scanning Voltmeter (Keithley 2700 equipped with a 40-channel multiplexer card model 7702) to measure the individual currents. The electrical schematics are shown in figure 5.2.

The experiment is controlled by a computer running a self written Labview program. The connections to the TRHX system and the instruments are made via a serial link and GPIB, respectively. The parameters and limits are read from a configuration file called *input file* (see table B.1). At the start of the measurements the program ramps up the voltage and records the IV curves of the sensors at the same time (see figure 5.3 for typical IV curves).

Then it reads the sensor currents derived from the voltage drops, temperature and humidity from the instruments periodically, displays the data online and writes an output file. It also handles the control of the electromagnetic valve to ensure that the humidity remains within the specified range. After the measurement is finished, the program shuts down the SMU voltage and writes an XML file for each tested sensor ready for insertion into the TrackerDB.

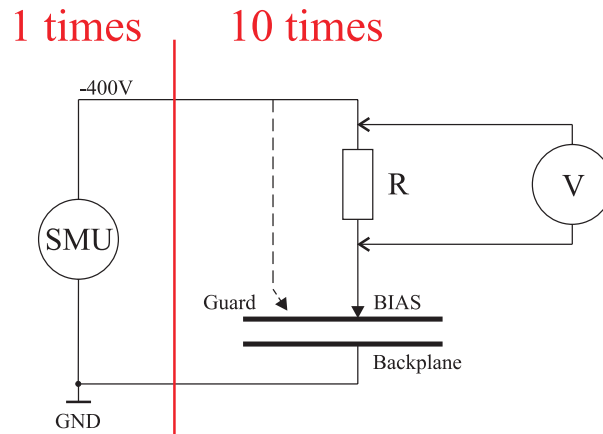


Figure 5.2: Electrical schematics of the longterm measurement setup. One SMU is connected to ten sensors with individual shunt resistors. The guard connection is foreseen, but not used in current configuration.

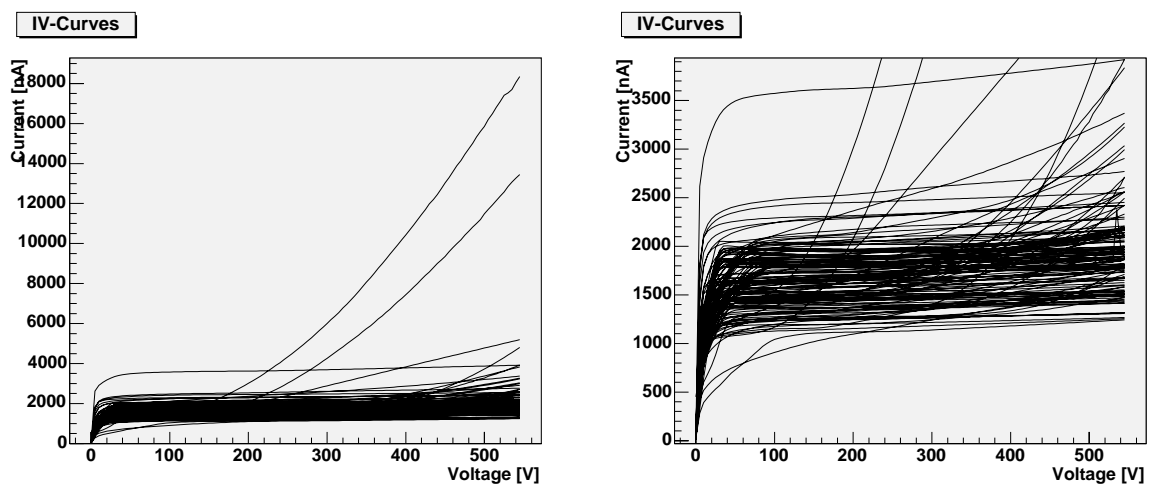


Figure 5.3: 143 IV curves of STM sensors taken with the longterm setup. A zoomed view is shown to the right.

5.1.2 Results

Fig. 5.4 shows a typical long term measurement of the dark currents of 19 sensors with a stable behavior over a period of 90 hours. Some sensors have been tested up to 120 hours. An unstable sensor behaviour is shown in figure 5.5. According to the contract with the companies and the technical specifications [21], *unstable* means a current increase of 30 % from its initial value.

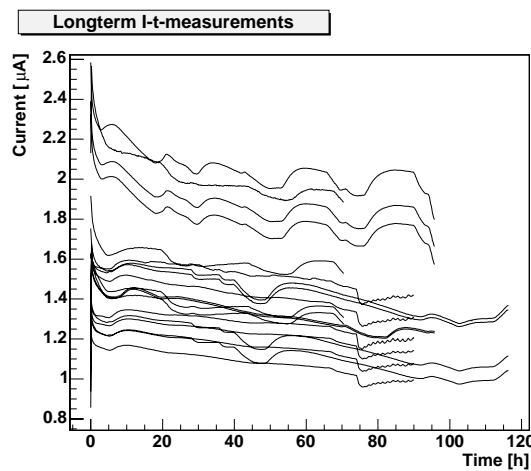


Figure 5.4: Typical longterm measurement of 19 sensors with a stable dark current behavior. The fluctuations are caused by the temperature dependence of the dark current since the box temperature is not controlled and thus subjected to day/night cycles.

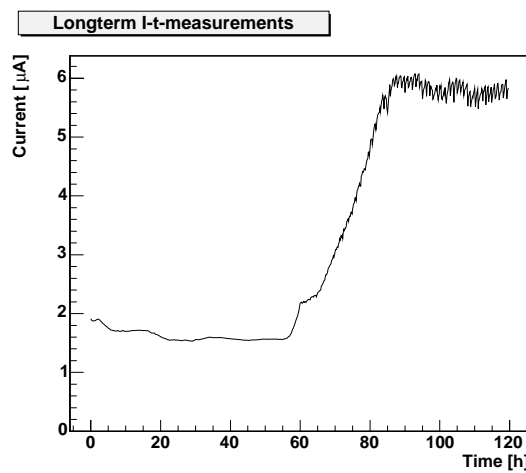


Figure 5.5: Behavior of an unstable sensor. The current typically stabilizes at a certain high level where fluctuations according due to humidity cycles occur.

The numbers in the next paragraphs are taken from TrackerDB. Up to now, 555 STM and 112 HPK sensors have been tested in Vienna. Together with 347 (STM) and 54 (HPK) sensors tested in Strasbourg, we present an analysis of the longterm stability.

For HPK, six of 166 sensors were flagged as unstable correlated to humidity in the TrackerDB. However, only one of those actually revealed a current increase above 30 %.

period	sensors tested	sensors failed	failure rate
old production	121	1	0.8 %
low R_{int} sensors	501	73	14.6 %
pre-production	280	17	6.1 %
sum	902	97	

Table 5.1: Overview of tested STM sensors divided into three different production periods.

The other sensors either had decreasing current or the fluctuations were within the specified range. These sensors are shown in figure 5.6. With one of 166 sensors failing, the failure rate is 0.6 %.

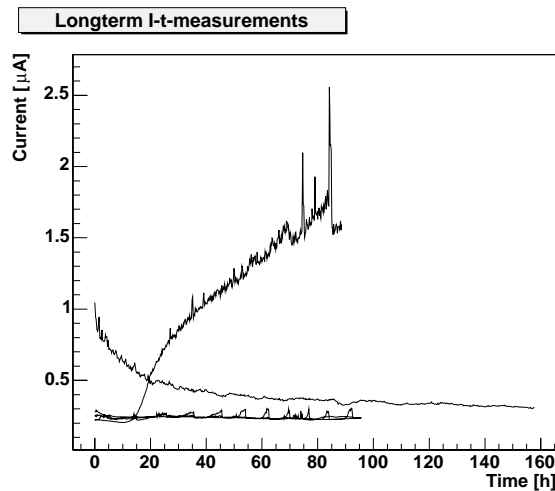


Figure 5.6: Dark current vs. time for six HPK sensors showing instabilities related to relative humidity. Only one sensor had an increase above 30 % from its initial value.

For STM it is not useful to summarise the sensors across the total production time, since we found different production periods with different properties at PQC. Thus, the analysis is divided into three periods:

1. before September 2003 (*old production*)
2. between September 2003 and March 2004 (*low R_{int} sensors*)
3. after March 2004 (*pre-production*)

The results are summarised in table 5.1 and the quality vs. measurement time is shown in figure 5.7.

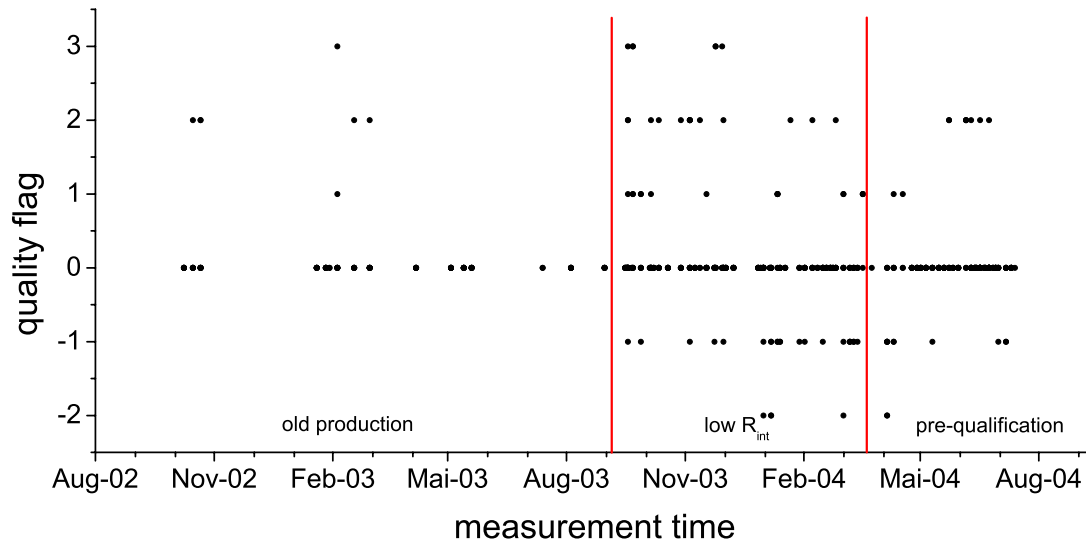


Figure 5.7: Quality flag vs. time for all tested STM sensors. Zero means no problem, negative values stand for unacceptable instabilities (e.g. current increased above limit of $10 \mu A$) and positive values of the quality flag correspond to instabilities related to humidity.

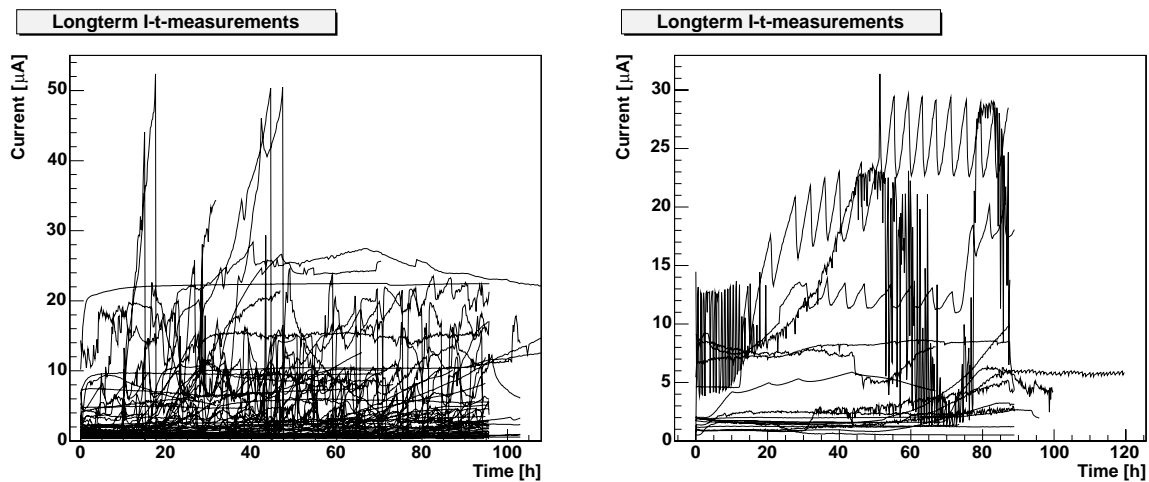


Figure 5.8: Longterm dark current behaviour of unstable STM sensors. *left*: low R_{int} period (73 sensors) *right*: pre-production period (17 sensors). The oscillations at high current levels are correlated to humidity cycles.

5.2 Longterm Tests at Operating Temperature

We performed a complementary long term test on a small sample of STM silicon sensors at CMS operating temperature of -10°C to validate the room temperature results. A further goal of this measurement was to estimate the maximum tolerable humidity in the tracker volume and to deduce if the *relative* or the *absolute* humidity causes the instabilities we have seen in the room temperature measurement. This test will not be part of the standard CMS quality control.

Absolute humidity (expressed as the mass of water vapor dissolved per air volume) is a measure of the actual amount of water vapor (moisture) in the air, regardless of its temperature. For example, a maximum of about 18.3 grams of water vapor can exist in a cubic meter volume of air with a temperature of 21°C , higher amounts lead to condensation. *Specific Humidity* refers to the amount of water vapor contained in a volume of air expressed as g/m^3). Absolute and specific humidity are quite similar in concept.

Relative humidity (r.H.) (expressed as a percent) also measures water vapor, but relative to the temperature of the air. Warm air can absorb more water vapor than cold air, so with the same amount of absolute/specific humidity, air will have a *higher* relative humidity if the air is cooler, and a *lower* relative humidity if the air is warmer (see figure5.9).

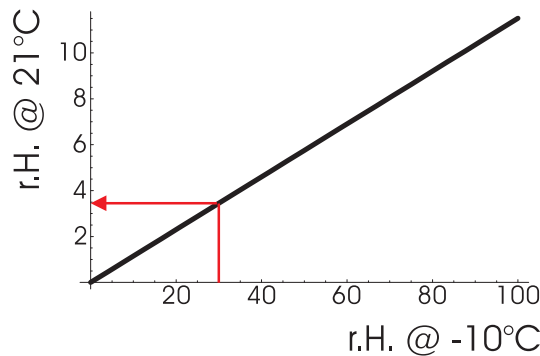


Figure 5.9: Correlation between the relative humidity at room temperature and at -10°C . A relative humidity of 30 % at -10°C corresponds to a value of 3.8 % at room temperature.

5.2.1 Setup Description

The cooling box used for this experiment [39] is equipped with two Peltier elements with 300 W electrical power each. Their waste heat is removed by a water-cooling system. The elements are driven by a power supply which is remotely controlled by the TRHX system. The silicon sensors are mounted on plates, which are in thermal connection to the two Peltier elements and also used for the backplane contact. As in the room temperature setup, the bias ring of each sensor is connected to a pad by wire-bonding. The electrical setup to reverse-bias the sensors and to measure the dark

currents is the same as for the room temperature setup. This box can be flooded with nitrogen gas or dry air to control the humidity.

5.2.2 Results

The experiment was started by cooling the box from room temperature to -10°C , applying the bias voltage of 400 V to the sensors followed by periodical dark current measurements. A decreasing dark current was observed according to the dropping temperature as expected (see equation 3.17). The evolution of the measured parameters is shown in figure 5.10. These tests were performed for 30 different STM sensors

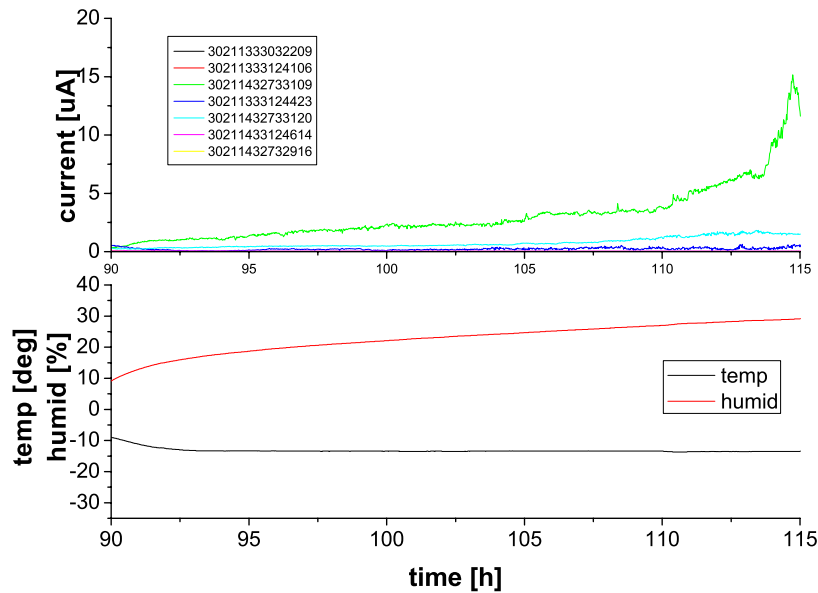


Figure 5.10: Dark current longterm behaviour of seven STM sensors operated at -10°C . Temperature (red) and relative humidity (black) are shown on the bottom plot.

so far. We observed the same current increase as at room temperature measurements at similar relative humidities. Thus, we concluded that the *relative* humidity causes this behaviour.

We crosschecked some sensors at both temperatures to compare the current saturation level. A typical result is shown in figure 5.11. The current value is almost the same, independently of the temperature. Thus, a temperature dependent bulk current is out of the question, and we concluded that it is a surface current.

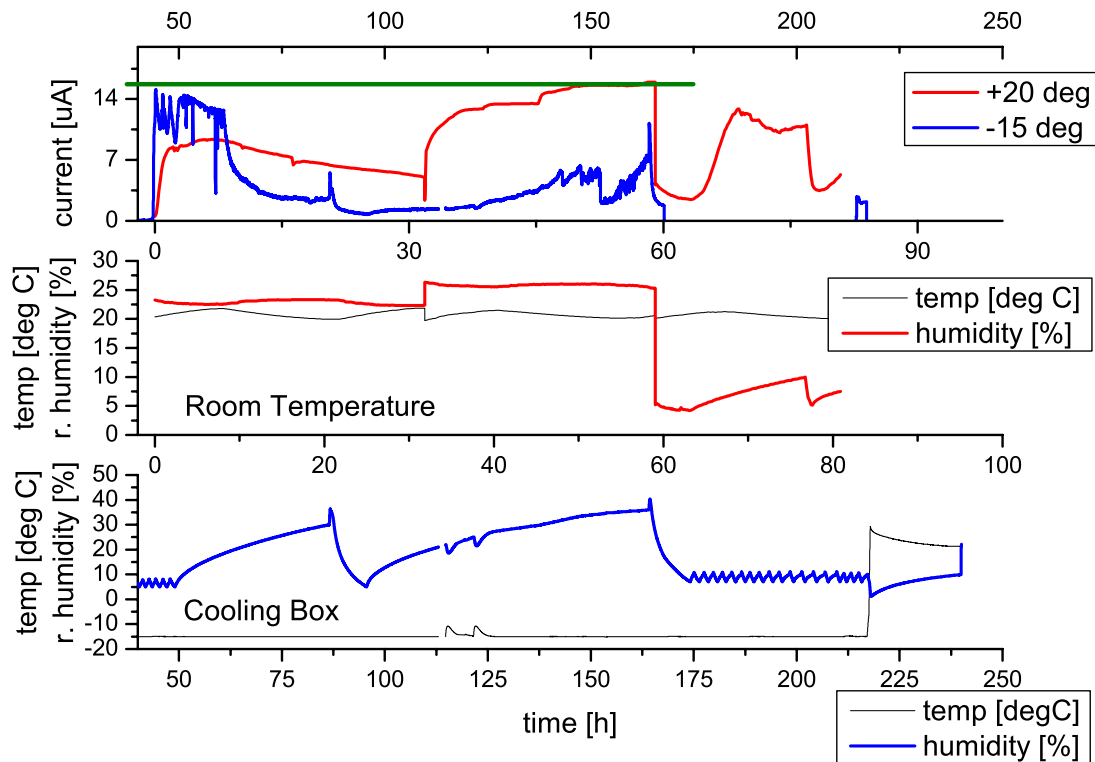


Figure 5.11: Comparison of the same sensor tested at room temperature and in the cooling box, where almost identical current levels were observed (green line).

5.3 Summary

We have seen that HPK sensors are quite stable across the complete production time. This was also true for STM sensors of the old production. After STM changed the fabrication process after September 2003, we got very high failure rates of almost 15 %, which dropped down to 6 % after April 2004. Unfortunately, this is still beyond the specified maximum failure rate of 1 %.

We learnt from the experiment at operation temperature that the instabilities caused by humidity are induced by a temperature-independent surface current, since we observed almost the same current at both room and cold temperature measurements. We also found that the relative humidity is the relevant moisture measurement in this context.

Chapter 6

Summary

The proton-proton collider LHC has been presented together with its physics aims, like the search for the Higgs particle, the investigation in CP-violation and heavy ion physics to prove the Standard Model of particle physics and explore possible extensions, like Supersymmetry.

Moreover, the CMS experiment with its components and especially the silicon tracker have been described to show the motivation for silicon radiation detectors and their properties like charge collection and other characteristics.

The design of the tracker and its silicon sensors and the necessary quality assurance facilities demonstrate the challenge to build such a large silicon detector device.

6.1 Process Quality Control

An elaborate setup has been developed in collaboration between HEPHY Vienna, INFN Florence and IReS Strasbourg to monitor the process stability of the semiconductor sensor production of the companies HPK and STM.

The hardware and the nine different measurements which are performed on teststructures – a set of different semiconductor devices produced together with the sensor on the same silicon wafer – are described in detail and the measurement procedure is presented.

After two years of operation the results are shown in diagrams comparing the two companies. While the HPK results look promising, stability problems of the manufacturing process at STM cast some doubts on the sensor stability during the planned ten years of operation in the harsh environment of CMS. Although STM addressed the issues we discovered, a stable production process during the whole production schedule was not achieved.

The setup itself was working very well. We were able to gather many information about the fabrication process of the companies and found some issues which would have caused serious operational problems if the sensors had been used in the CMS Tracker.

6.2 Longterm Validation

Longterm dark current stability was investigated on a sample of silicon sensors. Each sensor was observed for at least 72 hours on a setup developed to monitor the current behaviour of ten sensors in parallel under controlled relative humidity. STM sensors revealed unstable dark currents.

A comparison between measurements performed at room temperature and at -10°C – the operation temperature of the CMS tracker – showed a similar behaviour in both environments, which led us to the conclusion that a *relative humidity* above approx. 20-30 % leads to surface currents which saturate at unacceptably high levels.

6.3 Conclusion

Instabilities on a significant fraction of STM sensors observed in both PQC and LTV lead to the decision to minimize the number of STM sensors for the CMS Tracker. The remaining quantities will be produced by HPK.

Acknowledgements

Many people at HEPHY Vienna and in the CMS Collaboration directly or indirectly contributed to the work described in this thesis.

First of all, I express grateful thanks to Manfred Krammer for supporting me all the time and providing the opportunity to do this interesting work.

I would like to acknowledge the contribution all people involved in development and operation of the setups described in this theses. In particular, I would like to thank Anna Macchiolo (INFN Florence) and Jean-Charles Fontaine (IReS Strasbourg) for the fruitful collaboration and for their good conceptions to solve all the problems we encountered in the last years. Furthermore, I want to acknowledge the local support of Margit Oberegger and Dieter Uhl for performing most of the measurements and of Rudolf Eitelberger and Roland Stark for their mechanical work on the measurement setups and other hardware.

I want to express my thanks to our project leader Josef Hrubec for his support and Edmund Widl for his contribution to the data analysis, especially for providing VisualDB and other programs.

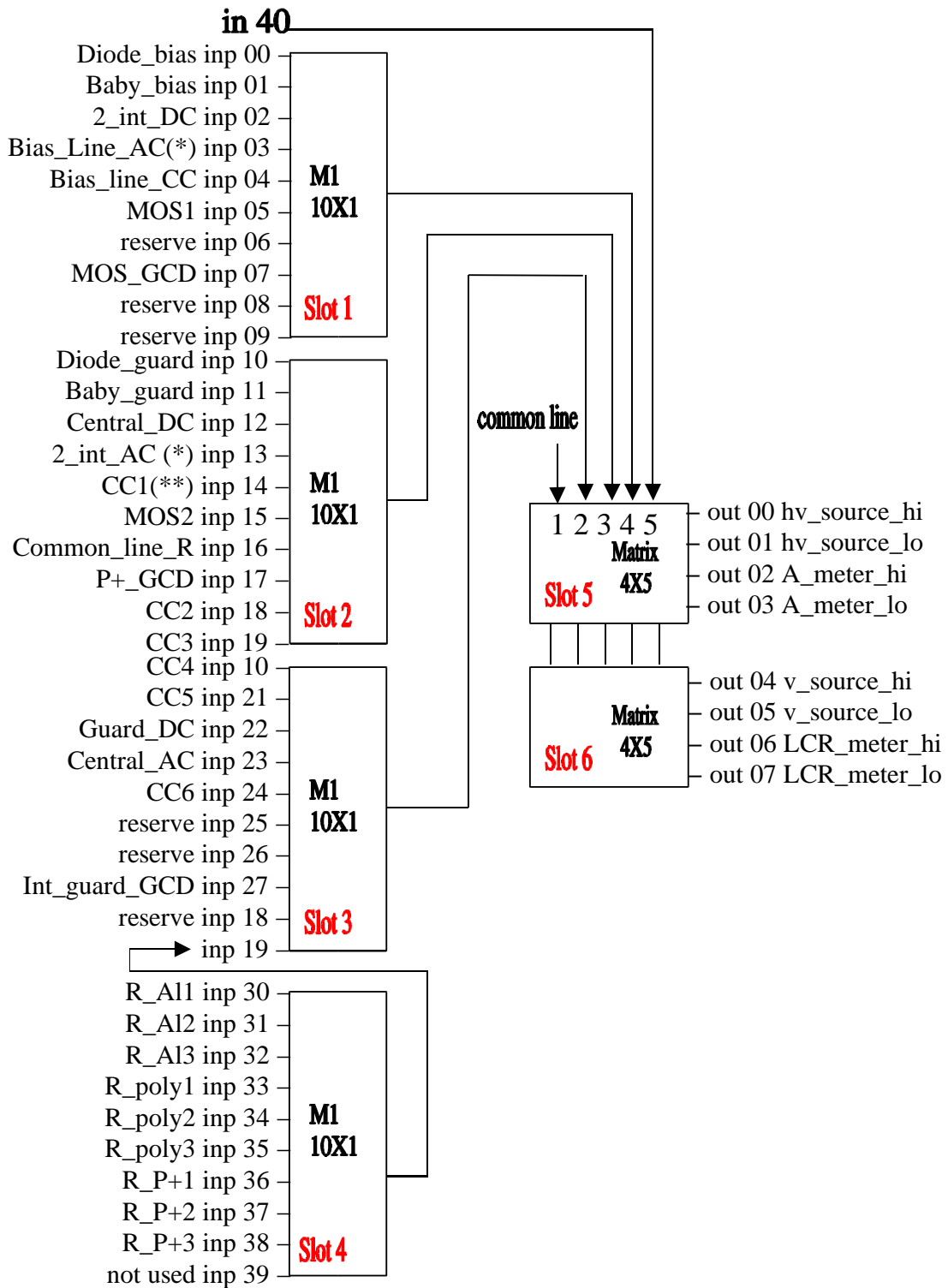
Moreover, I would emphasise the help of Markus Friedl not only in proofreading this thesis but also for his amicable support in private and work activities and thank Manfred Pernicka for many creative discussions.

I wish to express my big thanks to my parents for their continuous financial support during my study and – last but not least – to my girlfriend Birgit Forstner for her privations and considerateness during my exams and work for this thesis.

Appendix A

PQC Tables

A.1 Wiring Scheme



*: 6_ext-AC will be connected to Bias_line AC or to 2_int_AC

**: CC contacts are also used as I_diel contacts

Figure A.1: Schematics of the switching matrix.

Probe number	x (μm)	y (μm)	Structure	Pad Name	Shorts with probe number	Pin number on connector	Contact name (labview software)	switching matrix input number
1	0	550	ts_cap	P+	8	1	Bias_line_CC	04
N.C.	185	550	ts_cap	AC pad 1				
2	463	550	ts_cap	AC pad 2		61	CC1	14
N.C.	707	550	ts_cap	AC pad 3				
3	951	550	ts_cap	AC pad 4		2	CC2	18
N.C.	1195	550	ts_cap	AC pad 5				
4	1439	550	ts_cap	AC pad 6		60	CC3	19
N.C.	1683	550	ts_cap	AC pad 7				
5	1927	550	ts_cap	AC pad 8		3	CC4	20
N.C.	2171	550	ts_cap	AC pad 9				
6	2415	550	ts_cap	AC pad 10		59	CC5	21
N.C.	2659	550	ts_cap	AC pad 11				
7	2903	550	ts_cap	AC pad 12		4	CC6	24
N.C.	3147	550	ts_cap	AC pad 13				
8	3455	550	ts_cap	P+	1	58		
9	5133	550	Sheet	Common	19	5	Common_line_R	16
10	5337	550	Sheet	P+ pad 1		57	R_P+1	36
11	5627	550	Sheet	P+ pad 2		6	R_P+2	37
12	6081	550	Sheet	P+ pad 3		56	R_P+3	38
13	6326	550	Sheet	Al pad 1		7	R_Al1	30
14	6626	550	Sheet	Al pad 2		55	R_Al2	31
15	7089	550	Sheet	Al pad 3		8	R_Al3	32
16	7271	550	Sheet	Poly pad 1		54	R_poly1	33
17	7469	550	Sheet	Poly pad 2		9	R_poly2	34
18	7670	550	Sheet	Poly pad 3		53	R_poly3	35
19	7837	550	Sheet	Common	9	10		
20	12456	358	Surface	External guard		52	Ext_guard_GCD	
21	12748	358	Surface	P+		11	P+_GCD	17
22	14646	289	Surface	Al MOS		51	MOS_GCD	07

23	14938	358	Surface	Internal guard	12	Int_guard_GCD	27
24	17537	0	cap_ts_AC	Bias	32	Bias_Line_AC	03
25	17670	385	cap_ts_AC	3 first strips	26, 30, 31	6_ext_AC	03 or 13
26	17911	0	cap_ts_AC	3 first strips	25, 30, 31		
27	18033	385	cap_ts_AC	Strip 4	29	2_int_AC	13
28	18155	0	cap_ts_AC	Strip 5 (central)		Central_AC	23
29	18277	385	cap_ts_AC	Strip 6	27		
30	18399	0	cap_ts_AC	3 last strips	25, 26, 31		
31	18648	385	cap_ts_AC	3 last strips	25, 26, 30		
32	18778	0	cap_ts_AC	Bias	24		
33	21800	550	Baby	Guard	36	Baby_guard	11
34	22000	350	Baby	Bias	35	Baby_bias	01
35	43500	350	Baby	Bias	34		
36	43700	550	Baby	Guard	33		
37	47375	415	cap_ts_DC	Guard	41	Guard_DC	22
N.C.	47515	810	cap_ts_DC				
N.C.	47760	415	cap_ts_DC				
38	47880	810	cap_ts_DC	Strip 4	40	2_int_DC	02
39	48000	415	cap_ts_DC	Strip 5 (central)		Central_DC	12
40	48125	810	cap_ts_DC	Strip 6	38		
N.C.	48245	415	cap_ts_DC				
N.C.	48490	810	cap_ts_DC				
41	48615	415	cap_ts_DC	Guard	37		
42	52440	555	Diode	Guard	45	Diode_guard	10
43	52840	750	Diode	Bias	44	Diode_bias	00
44	55240	750	Diode	Bias	43		
45	55500	555	Diode	Guard	42		
N.C.	59500	555	MOS 1	Guard			
46	59900	750	MOS 1	Al	47	MOS1	05
47	62000	750	MOS 1	Al	46		
N.C.	62500	555	MOS 1	Guard			

N.C.	66500	555	MOS 2	Guard			
48	67000	750	MOS 2	AI	49	25	
49	69500	750	MOS 2	AI	48	37	
N.C.	70000	555	MOS 2	Guard			MOS2
							15

Table A.1: Allocation between the pins of the probe-card, the probecard connector, the input of the switching system and the contact number used in the acquisition software.

A.2 Input File

Process_v_71 18.05.2004 ProcessFileStructure_v_7		thin low r (HPK1)	thin low r (HPK234)	thick high r (HPK_THICK)	thick high r (STM)
IV	input ID	178	178	178	178
	start [V]	0	0	0	0
	stop [V]	700	700	700	700
	step_size [V]	5	5	5	5
	Voltage_1 [V]	450	450	450	450
	I_tot_max_at_V1 [uA]	1	1	1	1
	V_break_min [V]	500	500	500	500
	delay_time [s]	1	1	1	1
CV	input ID	695	696	154	154
	start [V]	0	0	0	0
	stop [V]	300	300	300	300
	step_size [V]	5	5	5	5
	frequency [kHz]	100	100	100	100
	signal_amplitude [mV]	100	100	100	100
	V_depl_min [V]	150	90	100	100
	V_depl_max [V]	250	250	260	260
	C_tot_min [pF]	6	6	3	3
	C_tot_max [pF]	11	11	7	7
	delay_time [s]	1	1	1	1
MOS	input ID	162	162	162	224
	start [V]	-5	-5	-5	-5
	stop [V]	20	20	20	20
	step_size [V]	0.2	0.2	0.2	0.2
	frequency [kHz]	75	75	75	75
	signal_amplitude [mV]	100	100	100	100
	C_tot_min [pF]	200	200	200	300
	C_tot_max [pF]	1400	1400	1400	600
	flat_band_Vmin [V]	0	0	0	0
	flat_band_Vmax [V]	3	3	3	10
	delay_time [s]	1	1	1	1
GCD	input ID	177	177	177	177
	bias [V]	5	5	5	5
	start [V]	5	5	5	5
	stop [V]	-20	-20	-20	-20
	step_size [V]	-0.5	-0.5	-0.5	-0.5
	surface_current_min [pA]	5	5	5	5
	surface_current_max [pA]	100	100	100	100
	delay_time [s]	1	1	1	1
R_poly	input ID	181	181	181	181
	Voltage_for_poly [V]	1	1	1	1

	R_poly_min [MOhm]	1	1	1	1
	R_poly_max [MOhm]	2	2	2	2
	delay_time [s]	1	1	1	1
R_alu	input ID	181	181	181	181
	Start_Voltage_for_Alu [mV]	5	5	5	5
	Stop_Voltage_for_Alu [mV]	25	25	25	25
	Step_for_Alu [mV]	5	5	5	5
	Alu_min [mOhm/sqr.]	10	10	10	10
	Alu_max [mOhm/sqr.]	30	30	30	30
	delay_time [s]	1	1	1	1
R_p+	input ID	181	181	181	181
	Voltage_for_p+ [V]	1	1	1	1
	p+ max [Ohm/sqr.]	400	400	400	400
	delay_time [s]	1	1	1	1
C_ac	input ID	134	134	134	140
	frequency [kHz]	75	75	75	75
	signal_amplitude [mV]	100	100	100	100
	C_ac_min [pF]	18	18	18	16
	C_ac_max [pF]	25	25	25	20
	delay_time [s]	1	1	1	1
C_int	input ID	674	674	674	684
	bias [V]	400	400	400	400
	frequency [MHz]	0.1	0.1	0.1	0.1
	signal_amplitude [mV]	100	100	100	100
	C_int_min [pF]	0.3	0.3	0.3	0.5
	C_int_max [pF]	1.3	1.3	1.3	1.3
	delay_time [s]	5	5	5	5
R_int	input ID	834	834	834	844
	bias [V]	20	20	20	100
	Start_Voltage_acr. [V]	-2	-2	-2	-2
	Stop_Voltage_acr. [V]	2	2	2	2
	Step [V]	0.2	0.2	0.2	0.2
	R_int_min [MOhm]	1000	1000	1000	1000
	delay_time [s]	1	1	1	1
IVdiel	input ID	179	179	179	179
	bias [V]	1	1	1	1
	start [V]	0	0	0	0
	stop [V]	-200	-200	-200	-200
	step_size [V]	-10	-10	-10	-10
	V_break_min [V]	120	120	120	120
	current_max_at_120V [nA]	10	10	10	10
	delay_time [s]	1	1	1	1
	[End_of_Input_File]				

Table A.2: PQC input file.

Appendix B

LTV Tables

B.1 Input File

Longterm_v.5

07.08.2002

LongTermFileStructure_v.4

Table_name	sensor_type	*		
LongtermValidation_Table	input ID	198		
			HPK	STM
Table_name	sensor_type	*	1.1	2.1
IvfromIT_Table	input ID	295	295	295
	start [V]	0	0	0
	stop [V]	550	550	550
	step size [V]	5	5	5
	delay time [s]	1	1	1
	Voltage 1 [V]	300	300	300
	I_tot_max @ V 1 [μ A]	5	5	5
	Voltage 2 [V]	450	450	450
	I_tot_max @ V 2 [μ A]	10	10	10
	V_break_min [V]	500	500	500
IT_Table	input ID	296	296	296
	Voltage [V]	400	400	400
	Total time [min]	5760	5760	5760
	Step size [min]	10	10	10
	I_tot_max [μ A]	10	10	10

[End_of_Input_File]

Table B.1: LTV Input File.

Bibliography

- [1] HEPHY, **Institute of High Energy Physics of the Austrian Academy of Sciences**, Nikolsdorfer Gasse 18, 1050 Wien, Austria (<http://www.hephy.at/>)
- [2] CERN, **European Laboratory for Particle Physics**, CH-1211 Geneva 23, Switzerland (<http://www.cern.ch>)
- [3] **LHC Conceptual Design**, CERN/AC/95-05, (1995)
- [4] D.E. Groom et al., **Review of Particle Physics**, The European Physical Journal C15 (2000) 1 (<http://pdg.lbl.gov>)
- [5] ALICE Collaboration, **Technical Proposal**, CERN/LHCC 95-71, December 1995
- [6] P.W. Higgs, **Phys. Rev. Letters**, 12, 132 (1964); **Phys. Rev. Letters** 145, 1156 (1966)
- [7] M. E. Haber and G. L. Kane, **Phys. Rep.** C117, 75 (1985)
- [8] A. D. Sakharov: **Violation of CP Invariance, C Asymmetry, and Baryon Asymmetry of the Universe**, JEPT Letters, Vol. 5 Nr. 1, S. 24, 1967
- [9] J. Christenson et al. **Phys. Rev. Letters** 13, 138 (1964)
- [10] M. Kobayashi and K. Maskawa, **Progr. Theor. Phys.** 49, 652 (1973); N. Cabbibo, **Phys. Rev. Lett.** 10, 531 (1963)
- [11] CMS Collaboration, **CMS Technical Proposal**, CERN/LHCC 94-38, December 1994
- [12] CMS Collaboration, **CMS Technical Design Report**, CERN/LHCC 98-6, April 1998 (<http://cmsdoc.cern.ch/cms/TDR/>)
- [13] CMS Collaboration, **Addendum to the CMS Tracker TDR**, CERN/LHCC 2000-016, February 2000 (http://cmsdoc.cern.ch/cms/TDR/TRACKER/tracker_addendum.pdf)
- [14] D. E. Groom et al., **Passage of particles through matter**, Review of Particle Physics, C15, 163 (2000)
- [15] M.Friedl, **The CMS Silicon Strip Tracker and its Electronic Readout**, Dissertation, Vienna, May 2001 (<http://friedl.hephy.at/diss/>)

- [16] L.D.Landau, **On the Energy Loss of Fast Particles by Ionization**, Collected Papers of L.D.Landau, Pergamon Press, Oxford, 1965
- [17] S.Ramo, **Currents Induced by Electron Motion**, Proceedings of the I.R.E. 27 (1939), 584-585
- [18] Gerhard Lutz, **Semiconductor Radiation Detectors**, Berlin [u.a.], Springer, 1999
- [19] S.M. Sze, **Semiconductor Devices - Physics and Technology**, Wiley, 1985
- [20] J.Närkönen et al., **Proecessing and recombination lifetime characterization of silicon microstrip detectors**, NIM A 485 (2002) 159-165
- [21] Technical Specification, **Supply of Silicon Micro-Strip Sensors for the CMS Silicon Strip Tracker (SST)**, IT-2777/EP/CMS
- [22] Hamamatsu Photonics K.K., Hamamatsu City, Japan
- [23] STMicroelectronics, Catania, Italy
- [24] J.-L. Agram et al., **The silicon sensors for the Compact Muon Solenoid tracker – design and qualification procedure**, NIM A, 517 (2004) 77-93
- [25] S. Albergo et al., **Optimization of the silicon sensors for the CMS tracker**, NIM A 466 (2001) 300-307
- [26] Frank Hartmann, **The CMS all-silicon tracker – strategies to ensure a high quality and radiation hard silicon detector**, NIM A 478 (2002) 285
- [27] TrackerDB, **CMS Tracker Construction Database System** (<http://cmsdoc.cern.ch/cmstrkdb/>)
- [28] Thomas Bergauer, **relay.pl – A PERL script to query the TrackerDB relay application** (<http://relay.hephy.at/>)
- [29] Edmund Widl, **VisualDB – A CMS Tracker DataBase Histograming Tool** (<http://visualdb.hephy.at/>)
- [30] **Istituto Nazionale di Fisica Nucleare, Sezione di Firenze**, Largo E. Fermi 2, 50125 Firenze, Italy
- [31] IReS, **Institut de Recherches Subatomiques** 23 rue du Loess, 67037 Strasbourg, France
- [32] Mesatronik S.A., Voiron, France (<http://www.mesatronik.fr/>)
- [33] Markus Friedl, **TRHX – A temperature and relative humidity measurement system** (<http://trhx.hephy.at/>)
- [34] **General Purpose Interface Bus a.k.a IEEE488**
- [35] G. Segneri et al., **Results with microstrip detecturs produced by STMicroelectronics for the CMS tracker**, NIM A 476 (2002) 729-733

-
- [36] C. Becker et al., **Gate-controlled diodes for characterization of the $Si-SiO_2$ interface with respect to surface effects of silicon detectors**, NIM A 444 (2000) 605-613
 - [37] E. Barberis et al., **Capacitances in silicon strip detectors**, NIM A 342 (1994) 90-95
 - [38] National Instruments, **Labview – Graphical Development Environment for Data Acquisition, Analysis, and Presentation** (<http://www.ni.com/labview/>)
 - [39] Manfred Pernicka, Markus Friedl, **Vienna Cooling Box**
(<http://cb.hephy.at/>)